Water Level Modulation of Wave Transformation, Setup and Runup over La Saline Fringing Reef

William Bruch [1*], Emmanuel Cordier [2], France Floc'h [3], Stuart G. Pearson [4,5]

[1]Mediterranean Institute of Oceanography (MIO - UMR7294), Université de Toulon, France
[2]Observatoire des Sciences de l'Univers de La Réunion (OSU-R), UAR3365, 97744 Saint Denis, France
[3]Université de Bretagne Occidentale, CNRS, Géo-Océan UMR6538, F-29280 Plouzané, France
[4]Faculty of Civil Engineering and Geosciences, Delft University of Technology, Delft, The Netherlands
[5]Department of Applied Morphodynamics, Deltares, Delft, The Netherlands

Key Points:

- Study of wave transformation over La Saline fringing reef, a natural coastal defence against Southern Ocean swell and cyclonic events
- As gravity waves dissipate over the fringing reef, significant energy transfer to infragravity and very low frequency bands occurs
- Wave setup and runup are greater for higher offshore wave height (H_{S0}) and lower water level. Modelled runup scales as ≈20% of H_{S0}

*Current address, 1 Rue de la Noë, Batiment N, 44300 Nantes

Corresponding author: William Bruch, william.bruch@mio.osupytheas.fr

Abstract

Coral reefs represent an efficient natural mechanical coastal defense against ocean waves. The focus of this study is the La Saline coral reef, located in the West of La Réunion Island in the Indian Ocean. The area is microtidal and frequently exposed to Southern Ocean swell as well as cyclonic events. The objective of this paper is to provide a better understanding of the coastal defense characteristics of the reef system for a range of Southern Ocean swell events and tides. Pressure sensors were placed across the reef to measure water level fluctuations and to determine gravity wave and infragravity wave components and their transformation across the coral reef. A numerical model (XBeach surf beat), validated using field observations, was used to deepen understanding of wave transformation, wave setup and runup. Field measurements and model outputs show that as gravity waves break over the reef, the reef acts as a low-pass filter. Study results also suggest frequency-dependent dissipation of infragravity waves by bottom-friction. The resulting wave-induced setup is found to be the dominant hydrodynamic component. The setup and runup are each 95% and 71% driven by the significant wave height (H_S) with which they increase, and transfer functions relating incident wave characteristics to reef system hydrodynamics are proposed. At a semi-diurnal tidal timescale, the setup and runup are in anti-phase, as the runup is highest in conditions of reduced wave dissipation on the reef flat, corresponding with high tides. These conditions also result in a lower wave setup.

Plain Language Summary

Coral reefs protect the coastline from ocean waves. The protective characteristics of reefs depend on factors such as coral health, water depth, oceanic and meteorological conditions, making them site dependent. La Saline fringing reef on La Reunion Island is frequently exposed to Southern Ocean swell and cyclonic events. Accompanied by numerical modelling efforts, pressure sensors placed across the reef allow to study water level fluctuations for a range of swell events and tides. Results reveal that waves transform as they break and dissipate over the reef; the energy of higher frequency and breaking gravity waves is transfered to lower frequencies. In La Saline, hydrodynamics are mainly driven by significant wave height. When water level over the reef is lower, gravity wave dissipation is highest, and the water level in the reef system rises. When the depth over the reef is higher, gravity wave dissipation is reduced, resulting in more gravity waves reaching the beach. Considering the predicted sea level rise in climate change scenarios, these results suggest that the protective capacity of the La Saline fringing reef could decline, thus altering reef hydrodynamics and sediment transport.

1 Introduction

Low-latitude and often low-lying islands are frequently located in oceanic regions prone to extreme natural events and disasters of hydro-meteorological origin, such as tropical cyclones, storms, flooding, and drought. In the context of global climate change, growing concern for the future of these environments has resulted in recent initiatives (e.g., UNESCO (2014)) for the building of small island resilience. Many of these tropical environments are bordered by coral reefs that are home to some of the most biodiverse and productive ecosystems on the planet (Pascal et al., 2016; Woodhead et al., 2019) and provide extremely valuable ecosystem services as a coastal defense against these events. An increasing number of studies indicate that up to 98% of incident wave energy is dissipated by coral reef systems (Brander et al., 2004; A.-C. Péquignet et al., 2011; Ferrario et al., 2014; Beetham et al., 2016).

Reef systems protect the coastline by inducing wave transformation in incident wave fields through wave-bottom interactions. Reef systems act as a low-pass filter, as wave energy dissipation mainly occurs in the gravity part of the wave spectrum (typically above frequency of 0.04 Hz) through mechanisms such as wave breaking in the surf zone and bottom

friction, especially important over rough and shallow reef flats (Lowe et al., 2005; Ferrario et al., 2014; Monismith et al., 2015). These physical processes are strongly related to the water level above the reef crest and to the bed friction (Lentz et al., 2016) which is regularly described by two coefficients in reef environments. The short period wave friction coefficient (commonly denoted f_w) describes the rate of gravity wave energy dissipation due to bed friction, and is strongly affected by the reef structural complexity (Harris et al., 2018). f_w ranges [0.1 - 0.5], with increasing friction for increasing coral complexity (Lentz et al., 2016). The friction coefficient (commonly denoted c_f) is associated with both the mean currents and the long period waves, and refers to the dissipation of energy in the mean current and wave-induced flow by the reef. c_f is commonly spatially varying, by depending on coral species density (among other properties) and water depth (Van Dongeren et al., 2013; Quataert et al., 2015; Pearson et al., 2017). These two coefficients, commonly indirectly calibrated or estimated from cross-reef wave measurements or numerical simulations, strongly depend on the characteristics of each individual study site, thus highlighting the importance of multiplying local *in situ* studies.

In coastal regions, the dissipation of incident gravity waves (0.04-0.25 Hz) - herein referred to as GW – results in increased water level over the reef as a result of wave-induced setup (Gerritsen, 1980; Vetter et al., 2010), resulting in the possible flooding of coastal areas. GW dissipation also contributes to the amplification of longer period wave components (Symonds et al., 1982; A. Pomeroy et al., 2012; Sous et al., 2019), which include infragravity (0.004-0.04 Hz) and very low frequency (0.001-0.004 Hz) waves - herein referred to as IG and VLF waves, respectively. IG wave generation is associated with the surf-zone-width-dependent breakpoint forcing mechanism, and the gravity wave group mechanism, the latter describing the release of free bound waves from GW envelopes during shoaling and breaking processes. The resulting IG waves have been shown to significantly contribute to bed shear in reef systems as well as overwash, potentially leading to damage to coral reefs (Baumann et al., 2019) as well as shoreline erosion (Bertin et al., 2018). VLF waves are identified as seiche-like and potentially resonating waves formed and amplified by non-linear wave transformation associated with wave-breaking processes (Péquignet et al., 2014; Gawehn et al., 2016; Sous et al., 2019). As GW dissipation over the reef flat is not usually complete, the remaining gravity wave components and the accentuated lower frequency wave components propagate across the reef system, driving runup, overwash, and resulting sediment transport (A. Pomeroy et al., 2012; Quataert et al., 2015; Cheriton et al., 2016). In strong swell events, GW, IG and VLF combined can strongly contribute to reef hydrodynamics, threatening shoreline and reef structural integrity.

The role of and need for coral reefs as a shield against such hazards is expected to evolve over time. Observations and climate predictions point towards global sea level rise as well as increasingly frequent and intense tropical storms and cyclones (Grady et al., 2013; Merrifield et al., 2014; McLean & Kench, 2015; Quataert et al., 2015; Storlazzi et al., 2015; Cheriton et al., 2016; Beetham & Kench, 2018). Projected increases in carbon dioxide and temperature combined with anthropogenic stresses are expected to lead to the loss of much of the world's coral reefs by the end of the 21th century (Hughes et al., 2003, 2017, 2018; Hoegh-Guldberg et al., 2007; Camp et al., 2018), and with them the natural coastal protection they provide against increasingly severe wave-driven flooding events in tropical islands and atolls (Sheppard et al., 2005; Principe et al., 2011; Harris et al., 2018). If the underlying physical processes of coral reef shore-protection are increasingly understood, their accurate quantification is hindered by the high heterogeneity of reef and shoreline morphologies (e.g., Baldock et al. (2014); van Dongeren et al. (2017)) as well as meteorological and oceanic conditions (e.g., Lowe and Falter (2015)). Furthermore, Owen et al. (2016) noted that small variations in island topography and land use also influence wave-driven flooding and associated impacts. Responding to this need for flood predictions over reefs of widely varying shape and size but lacking sufficient field measurements, Pearson et al. (2017) numerically simulated over 174,000 combinations of different reef morphology and physical forcing. They showed that waves, water levels and reef width are the most

important parameters to consider when predicting reef wave heights and run-up. However, there is still a need for more detailed field observations of such sites (Pearson et al. (2017)). Fringing reefs are particularly interesting as their narrow and shallow characteristics can result in the highest setup and runup at the shore front.

In coral reef systems, the wave setup appears to be modulated by the water level (Bonneton et al., 2007; Becker et al., 2014; Sous et al., 2020). Under certain coral reef configurations, water level is either the dominant influence on lagoon hydrodynamics (Chevalier et al., 2015), or at least modulates dynamics primarily driven by oceanic waves (Becker et al., 2014). In light of this, this study addresses the question of the wave dissipative capacity and the physical forcing of hydrodynamic processes on La Saline (La Réunion) fringing reef. Since the wave dynamics and tidal fluctuations are shown to be specific to each reef system, this study uses a combined approach between field observations and 1-D numerical modelling (XBeach surfbeat model, D. Roelvink et al. (2009)) in order to investigate the dissipative capacity of this fringing reef. Here, field measurements are made to describe water levels offshore and inside the reef, to estimate the GW dissipation due to bottom friction on the reef, study water level variations, and to validate the numerical model. This model is in turn used to predict run-up at the shore. The main objective is to provide transfer functions linking incident waves, tide, setup and runup, which are required by the scientific and engineering community and therefore decision and policy makers for coastal zone management.

2 Field measurements and data analysis

2.1 Study area and experiment design

La Saline fringing reef is located on the western coast of La Réunion Island in the South Western Indian Ocean (SWIO) (Fig. 1a and b), leeward of the prevailing winds, and is seasonally exposed to oceanic swell generated by tropical cyclones during the austral summer (November to March) or by winter austral swell events (April to October). The winter austral swells are generated by distant storms induced by strong atmospheric depressions that occur in the Southern Ocean at a distance of 3000 - 4000 km from La Réunion (Davy et al., 2016). These swells may produce significant damage to coastal infrastructures such as roads, houses, harbors, but also to the natural coral reef protecting part of the western coast of La Réunion (Cordier et al., 2012). At the study site, the fringing reef is around 500 m wide, backed by a sandy beach of approximately 30 m with a 1:10 slope (Fig. 1b and c). From the beach to the reef flat (herein RF), the back reef (approximately 200 m wide, herein BR) has a mean water depth of approximately 1 m and is essentially made up of biodetrital sands occupied by scattered coral colonies. The reef flat has a water depth of about 0.5 m and can sometimes be exposed at low tide. Beyond the RF, the reef-slope (hereafter RS, with a slope nearing 1:15) or fore reef has a rough topography made of individual coral heads, boulders and spurs that reach 20 m depth. The reef crest (0.3 m depth below mean sea level (MSL)) marks the transition between the RS and the RF, and is where the oceanic incident waves break. The tides around La Réunion are mixed, mainly semi-diurnal with a mean tidal range of 0.37 m (Cordier et al., 2013).

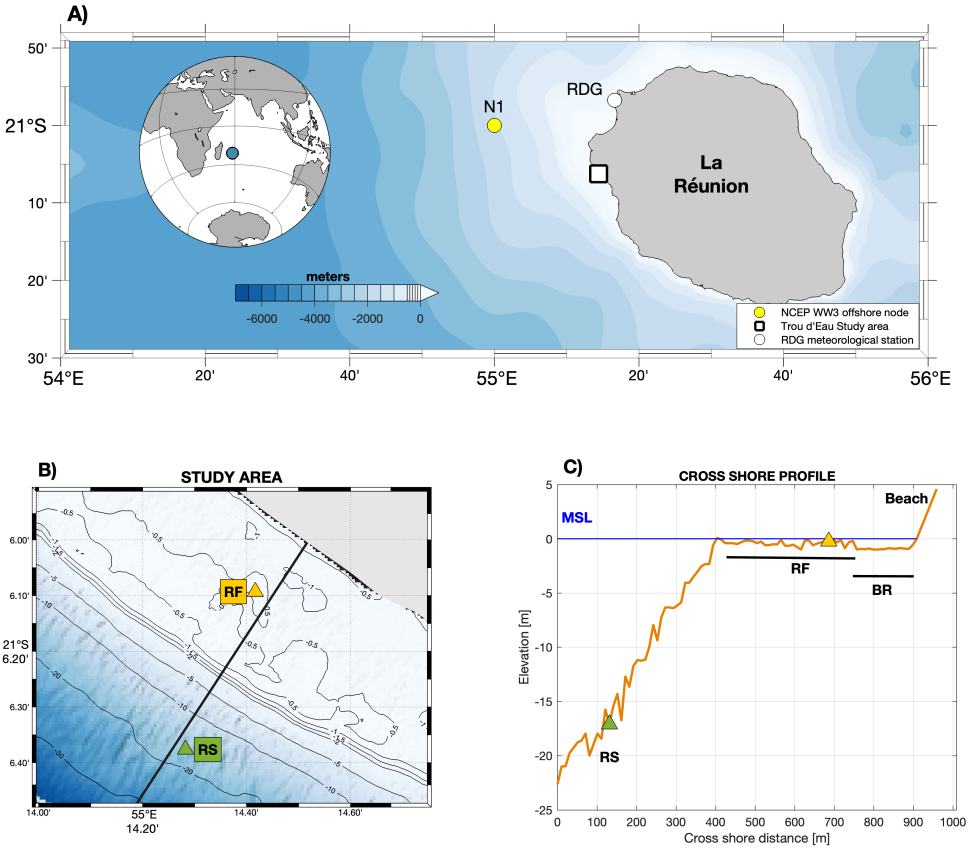

Figure 1. A) Location of La Reunion island in the South Western Indian Ocean, the studied area is indicated by the white square, the MeteoFrance meteorological station RDG is indicated by a white dot, B) zoom on the fringing reef indicating the bathymetry of the fringing reef and the position of the cross-shore transect with the two measurement points on the reef flat (RF) and on the reef slope (RS) separating the open ocean from the back reef (BR), C) detailed vertical profile of the cross-shore transect used for the 1D XBeach modelling.

A cross-shore transect of bottom fixed Ocean Sensor System Instrument wave gauges (OSSI) combined with an upward-facing Nortek Aquadopp current profiler (AQP) was deployed for 53 days across La Saline reef from 13-Mar-2017 to 05-May-2017 (Fig. 1b). The two OSSI pressure sensors were configured to continuously record the sea states at a sampling frequency of 10 Hz and the AQP was configured in an hourly burst mode, recording 2048 samples at 2 Hz (≈18 minutes). The RS station was located on the reef slope at a mean depth of 19.5 m and combined the OSSI with the AQP. The RF station was located in the reef flat at the transition zone with the back-reef, at a mean depth of 0.9 m.

These field data were used to quantify the wave heights in each frequency-band of the wave spectrum, the shortwave dissipation processes due to bottom friction across the reef flat and the induced setup for different conditions of oceanic incident wave heights and tides. The runup, in turn, was extracted from the numerical modeling (see Sect. 3).

2.2 Data analysis

The OSSI pressure data were corrected i) from atmospheric mean sea level pressure recorded at the MeteoFrance station 'La Rivière Des Galets' (≈20 km northward, RDG on Figure 1a) and ii) non-hydrostatic pressure following linear wave theory (Hom-ma et al., 1966; Bishop & Donelan, 1987). The water depths h were extracted from the total signal using a second-order Butterworth low pass filter with a cut-off frequency at 6 hours in order to keep the tidal fluctuations, and averaged over 10 minutes. The residual high frequency signal was kept for spectral analysis in order to retrieve the energy density spectrum of the sea state $E(f)$ for each of the following 3 frequencies bands: gravity waves (GW, 0.04-0.25 Hz), infragravity waves (IG, 0.004-0.04 Hz) and very low frequency waves (VLF, 0.0006-0.004 Hz). The Fast Fourier Transform (FFT) method accompanied with Hamming windowing was used and applied over 4096 continuous data points (nfft) (≈ 7 min) for GW, and over 32768 (nfft) (≈ 55 min) for IG and VLF waves. Finally, to avoid information loss at the edge of each data subsample, a moving average was performed spanning 30 minutes for GWs and 3 hours for IG and VLF waves, with 50% overlap (Pierson & Marks, 1952). The AQP data at the RS sample location were finally used to compute incident wave height, peak period and direction using the PUV method (Pedersen, 2002).

The spectral parameters significant wave height H_S, root-mean-square wave height H_{RMS}, and the mean energetic period $T_{m0,-1}$ were calculated in each frequency band according the equations $H_S = 4\sqrt{m_0}$, $H_{RMS} = \sqrt{8m_0}$ and $T_{m0,-1} = \frac{m_{-1}}{m_0}$ where m_n is the n^{th} order moment of the energy density spectrum of the sea state $E(f)$ such that $m_n = \int_0^\infty E(f) f^n df$ (Holthuijsen, 2010). The observed setup in the reef flat η_{RF} was computed from the 10 min averaged water depths h_{RS} and h_{RF} for the RS and RF location respectively, following the Vetter et al. (2010) formula:

$$\eta_{RF} = h_{RF} - h_{RS} - (bt + c) \tag{1}$$

where t is time, b and c are obtained from a regression of the form:

$$h_{RF} - h_{RS} = aH_{RMS}^{RS} + bt + c \tag{2}$$

with H_{RMS}^{RS} the root-mean-square wave height at the reef slope location. This procedure is used to account for relative pressure drift over time between the two sensors, and to select a reference level offset, c, so that the reef flat setup is null $\eta_{RF} = 0$ when the reef slope RMS wave height is null $H_{RMS}^{RS} = 0$. The strength of this relation is quite good with $R^2 = 0.95$, allowing for an accurate estimate of the vertical position of the RS sensor that is $c = 18.7$ m below the RF sensor position.

In order to compute absolute sea level variations according to a referenced datum, an accurate estimate of the vertical position of the pressure sensors is necessary. We used the bathymetric dataset illustrated in Fig. 1 projected in the WGS84-UTM40S coordinate system and using a local vertical datum reference (IGN89) that corresponds to the mean sea level (MSL). This bathymetric chart is a merged product between a 1 m high resolution topography and bathymetry issued from LIDAR acquisition and a 0.4 m high resolution bathymetry of the shallower parts of the reef issued from hyperspectral images (Mouquet et al., 2016; Ropert Michel et al., 2016). The localization of the reef flat sensor on this gridded data indicates a vertical height of 0.9 m below datum, i.e. ZRF = -0.9 m. Considering the previously calculated relative position of the RS sensor to RF sensor of 18.7 m, the vertical position of the RS sensor below datum can be easily deduced, i.e. ZRS = -19.6 m. Finally, the location of the reef crest was also extracted from this bathymetric chart as the highest point between the reef slope and the reef flat, resulting in a reef crest located at a distance D = 280 m from the RF sensor and a ZRC = -0.3 m below datum.

2.3 Overview of oceanic conditions during field observations

In addition to the field measurements made at RS station with the AQP, external data issued from the global WaveWatch III (hereafter WW3) hindcasts model produced by the National Oceanic and Atmospheric Administration (NOAA) and National Centers for Environmental Prediction (NCEP) were used. The modelled significant wave height, peak period and direction were extracted at a node of the model located west of La Réunion Island, at latitude 21°S and longitude 55°E, illustrated by the node N1 on Fig. 1a.

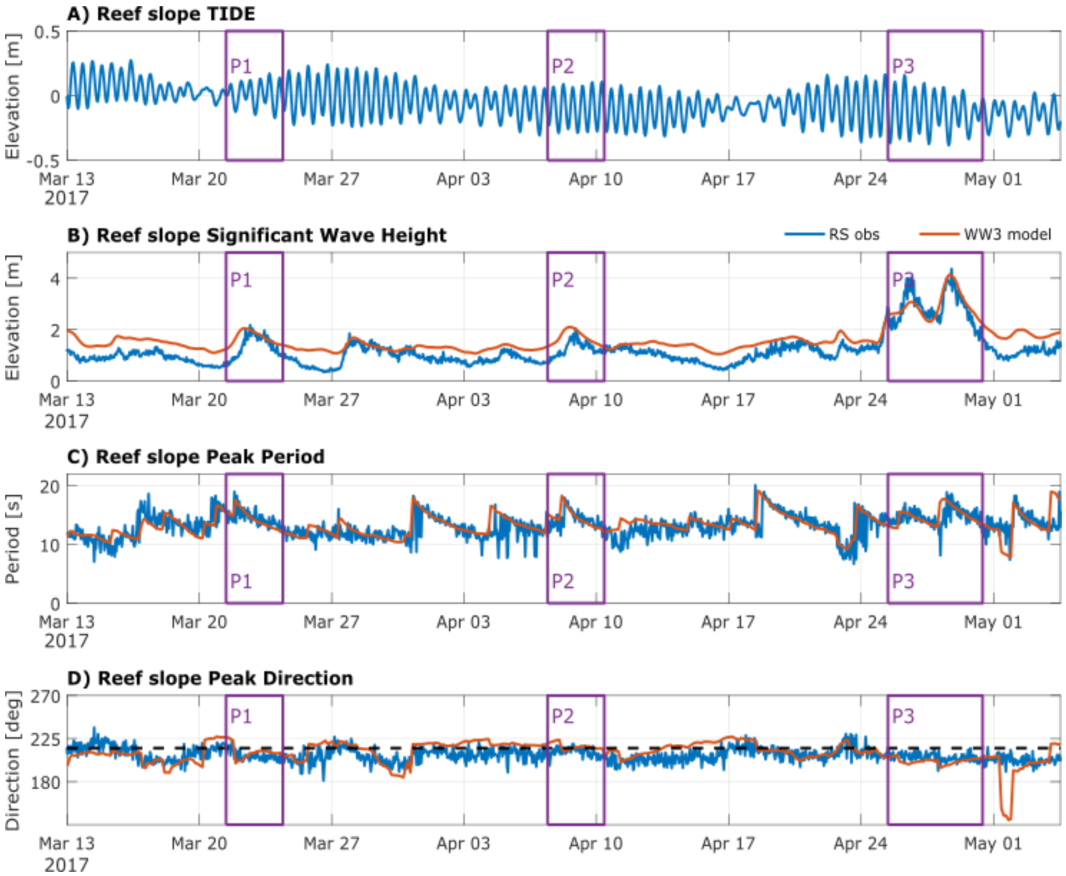

Figure 2. Oceanic forcings during the field experiment. A) offshore tide measured at the reef slope with the AQP, centered on the local datum reference level. B) significant wave height (H_S). C) wave peak period (T_P). D) wave peak direction (θ) clockwise from north. Shore-normal direction is 218° (black dashed line). The WW3 NCEP model data are plotted in red and the measured data at RS in blue. See Fig. 1a for the location of the WW3 NCEP model node N1 and the RS station.

During the 53 days of the experiment, the tide is a typical microtidal regime with a maximum tidal range around 50 cm, a minimum around 4 cm, and a mean tidal range of 27 cm (Figure 2A). The mean tidal level slightly decreased all along the field experiment from +0.1 m to -0.1 m relative to the reference datum. The wave climate is characteristic of the SWIO during this transition period between the austral summer and austral winter. The linear fit between the modeled and observed data at the reef slope is quite good with R^2 = 0.87 and a root mean square error of 0.19 m when comparing wave heights, and R^2 = 0.43 and a root mean square error of 1.44 s when comparing peak period. However, the WW3 results slightly overestimate the significant wave heights during most of the weather conditions, and underestimate the wave heights during the double-peaked strong swell event

at the end of April. These differences are likely due to the fact that the model is configured for the offshore wave dynamics and does not account for local wave energy dissipation or shoaling at the shore. The peak wave direction for the local measurements are mainly centered around 220°N which corresponds to the shore normal direction that is around 218° (nautical convention). The differences between the WW3 peak direction and local measurements (Fig. 3D) are probably due to local wave refraction processes unaccounted for in the model. The low standard deviation of the measured peak direction at the reef slope (std=±7°) over the whole period gives us confidence in assuming that the incoming waves are shore normal, and can justify the choice of a 1-D numerical modeling that is explained in the next section (see Sect. 3).

Table 1. Periods of interest and corresponding offshore conditions at the local measurements RS. For each period, the Mean Tidal Range (MTR) is the difference between the mean high water and mean low water levels, the Full Tidal Range (FTR) is the difference between the higher and lower water level, the Still Water Level (SWL) is the height of the offshore mean water level relative to the IGN89 datum. The MTR, FTR and SWL are expressed in meters. The wave characteristics are described by the measured maximum values of the significant wave height H_S (meters) and peak period T_P (seconds), and the mean peak direction D_P (degrees) with its standard deviation.

Period	Dates	MTR (m)	FTR (m)	SWL (m)	max (H_S) (m)	max (T_P) (s)	mean (D_P) (°)	STD (D_P) (°)
P1	22–24 March	0.21	0.34	0.01	2.17	19	207	±4
P2	08–10 April	0.30	0.40	-0.09	2.04	17.9	211	±5
P3	26–30 April	0.34	0.54	-0.13	4.36	18.9	206	±4

Three periods of interest were identified corresponding to two moderate swell events marked P1 and P2 and a stronger event marked P3 on Fig. 2A. The incident oceanic forcings measured at the reef slope station that allowed to characterize each period are presented in Table 1. Periods P1 and P2 are characterized by a moderate south-south-west swell event with a maximum significant wave height H_S around 2 m and maximum peak period T_P of 19 s P1 and 17.9 s for P2, respectively. The tidal modulations during P1 are relatively weak, characterized by a transition from neap to spring tides, with low mean (21 cm) and full (34 cm) tidal ranges, and a SWL of +0.01 m relative to datum. The tide for the period P2 is characterized by a spring tide with greater MTR (30 cm) and FTR (40 cm) but a lower SWL (datum -0.09 m). The period P3 is characterized by a strong swell event coming from the south-south-west, occurring at the end of a spring tide (MTR = 34 cm and FTR = 54 cm), with SWL a still water level of datum -0.13. This swell event has two successive peak events with measured significant wave heights of 4.1 m and 4.36 m and peak periods of 17.1 s and 18.9 s, respectively. These 3 events were selected in the scope of this study because they highlight highly energetic wave conditions under varying tidal and still water levels on a reef system. Doing so highlights the role played by the reef to reduce wave energy nearshore, focusing on wave transformation and propagation across a reef flat, and setup and runup induced at the shore.

In the following, the significant wave height H_S is most often used to describe wave height. To simplify the notations providing information of the sample location and the wave frequency band of interest, the signficant wave height is systematic unless specified otherwise (e.g. H_{RMS}). For example, the significant wave height of gravity waves measured at the wave slope is written H_{GW}^{RS}.

3 The numerical model

3.1 Model description

The XBeach model is used to reproduce the physical processes in the La Saline fringing reef and to predict wave runup, the latter not having been measured in this study. Initially developed for mild-sloping sandy beaches (D. Roelvink et al., 2009), the applicability of the XBeach model in reef environments and for steep reef bathymetry has been widely tested and validated in the literature (Pearson et al., 2017; van Dongeren et al., 2017; Harris et al., 2018; Storlazzi et al., 2018; Rueda et al., 2019; Quataert et al., 2020). XBeach can be run in short wave-averaged mode (surfbeat) or short wave-resolving mode (non-hydrostatic). The XBeach surfbeat mode (XBSB) resolves the wave energy variations on the wave-group scale which drives IG and VLF long- wave motions but is short-wave averaged (D. Roelvink et al., 2009). The XBeach non-hydrostatic mode (XBNH) resolves all wave motions and computes the depth-averaged flow due to waves and currents using the nonlinear shallow water equations including a non-hydrostatic pressure correction term (D. Roelvink et al., 2018). Both modes predict runup with similar error (Quataert et al., 2020).

In the present study, the model was run in XBSB mode on a 1D domain with a primary focus on cross-reef wave processes. Lashley et al. (2018) compared 1D modelling of XBSB and XBNH in a laboratory experiment that reproduced a fringing reef and, found that if both model configurations are able to accurately predict wave setup and extreme runup, XBSB seems to give better results. Quataert et al. (2015) also demonstrated that a 1D-XBSB model configuration produced good conservative estimates of the induced infragravity waves and corresponding runup while considering a shore-normal forcing wave field, with the benefit of significantly reducing computational costs relative to the XBNH configuration. Since the measured reef slope data has shown little directional variability of the incident waves (std=$\pm 5°$, cf. Sect. 2.3 and Fig. 2D), the wave direction can thus be considered to have negligible impact on cross-reef dynamics, and the incident wave field is then estimated normal to the reef. Consequently, this 1D-XBSB configuration appears thus suitable for our study since such a configuration has been demonstrated able to reproduce key reef hydrodynamical processes.

3.2 Model configuration and calibration

The bathymetric dataset described in Sect. 2.2 was used as reference data for the XB configuration. The original dataset is a bathymetric grid with a 0.4 m high resolution that is likely to introduce numerical instabilities due to spikes in the bathymetry resulting from the complex nature of the reef. To avoid a considerable increase in the modeling time and numerical instabilities, the mesh convergence step has led to a suitable model grid resolution of 10 meters and smoothed using a two-dimensional moving average with 20 m window size. The resulting 2D grid is illustrated in Fig. 1B, the cross-shore profile extracted from this grid and used in the 1D-XBSB model is presented in Fig. 1C. Since the bathymetric product focused only on the submerged part of the fringing reef, and to avoid overtopping up to the model land boundary, the topography of the beach face has been artificially prolonged considering a beach slope of 1:10 up to 5 m above the IGN89 datum, highest vertical location of the beach profile, in correspondence with beach profiles available for this area (data not shown, c.f., Mahabot et al. (2017)). The hourly averaged tidal water levels and the incident wave spectra recorded at the reef slope OSSI pressure sensor are used to force the model. The tidal variations were applied over the entire domain, while the incident gravity waves spectra were applied at the offshore boundary with frequencies ranging from 0 to 0.25 Hz using a 1.5×10^{-3}Hz discretization. A one-dimensional absorbing-generating weakly reflective condition was applied at the offshore and land boundaries, while a Neumann condition was used on the lateral sides of the domain.

A critical step in modeling reef hydrodynamics is the parameterization of the wave energy dissipation in rough reef environments. In the XBSB mode the dissipation is decom-

posed in a wave dissipation coefficient (α), gravity wave friction coefficient (f_w and mean currents and IG waves friction coefficient (c_f). The parameterization of these coefficients was deeply investigated for reef systems and studies indicate that f_w should be at least an order of magnitude greater than c_f (Lowe et al., 2007). The short-wave friction coefficient f_w appears as a factor of key importance for the assessment of the wave energy dissipation, since Harris et al. (2018) directly linked this factor to the cover of living corals and the structural complexity of the coral reefs. A number of theoretical and empirical values of f_w have been proposed in the literature, often ranging between f_w=0.1 and f_w=0.5, with increasing friction for increasing coral complexity (Lentz et al., 2016; Harris et al., 2018), and sometimes reaching exceptionally high values such as f_w=1.8 in a north Pacific atoll (Monismith et al., 2015) or even f_w=5.0 on coral reef platforms in the Red Sea (Lentz et al., 2016). The gravity wave friction and the bed friction coefficients were calibrated in order to provide the best fit between the simulated wave parameters and setup over the reef flat compared to pressure sensor data for the largest set of conditions. The optimal values were found to be $f_w = 0.3$ and a depth-dependent Manning formulation $c_f = \frac{gn^2}{h^{1/3}}$ with $n = 0.02$, g the gravity constant, and h the water level. This leads to spatially and time varying c_f-values ranging [0.005-0.02] at the reef crest according to the tidal variations. Best results were also found with the breaking formulation proposed in (J. A. Roelvink & Brøker, 1993), where wave dissipation is proportional to H^2, and the wave dissipation coefficient α and the breaker index γ are set to the model default value ($\alpha = 1.0$ and $\gamma = 0.55$).

3.3 Data processing and model validation

The XB wave-induced setup, the IG and VLF wave heights were calculated using the same methods as used for the observed data and described in Sect. 2.2 (see Equ. 1 for setup and spectral analysis). Subsequently, the model results were post-processed to compute 10-min water levels, setup and root-mean-square wave heights H_{RMS} for GW, IG and VLF waves, at RS and RF instrument locations. Finally, the modeled significant wave heights H_S were deduced from H_{RMS} according to the equation $H_S = \sqrt{2}H_{RMS}$ considered valid when assuming Rayleigh-distributed wave heights.

To qualify the accuracy of the model configuration, we used the observed setup and significant GW, IG and VLF wave heights at the reef flat station, and computed three statistical parameters, the coefficient of determination R^2, the Root Mean Square Error ($RMSE$) and the $Bias$:

$$R^2 = 1 - \frac{\sum_{i=1}^{n}(O_i - P_i)^2}{\sum_{i=1}^{n}(O_i - \underline{O})^2} \tag{3}$$

$$RMSE = \sqrt{\frac{1}{n}\sum_{i=1}^{n}(O_i - P_i)^2} \tag{4}$$

$$Bias = \sum_{i=1}^{n}\frac{(O_i - P_i)}{n} \tag{5}$$

where P_i and O_i are the i^{th} predicted and observed data respectively, $\underline{O}$ denotes the temporal mean of the observed data, and n is the total number of measurements.

Finally, the wave runup was computed by the numerical model at 1 Hz output frequency over the entire study period. In the present study, runup is mainly associated with the longer waves that are fully resolved in the XBSB mode. The short wave swash is not fully resolved in present study simulations. This assumption holds as a result of the high dissipation of short wave energy over the reef flat in most reef systems.

4 Results

4.1 Wave spectra observations

The wave spectra for the 53-day observations on the reef slope and the reef flat are illustrated in Fig. 3. The left panel of the plot shows the time series of observed power spectral densities, whilst the right panel shows the spectra temporal means over the study period, with black dashed lines at 0.004 and 0.04 Hz, highlighting the boundaries between the VLF, IG and GW frequency bands. The 3 periods of interest P1, P2 and P3 are also indicated by purple boxes. First, the temporally averaged spectra (Figs. 3b and 3d) shows that the limit that was fixed between the GW-IG bands (limit at 0.04 Hz) and the IG-VLF bands (limit at 0.004 Hz) appears to be a good choice in our study since the average spectrum reveals a local minimum of energy at these frequencies.

The gravity waves are almost totally dissipated while the waves break and propagate across the reef, characterized by a strong reduction of the spectral power density between RS and RF (Figs. 3a and 3c). The reef clearly acts as a low-pass filter maintaining energy in the IG band on the reef flat. Over the entire study period, the presence of a double peak in the IG band is observed, as also observed during specific events, with a first peak at 0.0076 Hz ($\approx$ 2 min) and a second peak at 0.0150 Hz ($\approx$ 1 min), possibly implying harmonic behavior. On the reef flat (Fig. 3d), the maximum of energy in VLF band is more than twice the maximum of energy in the IG band, with a large peak of energy at 9.10^{-4} Hz ($\approx$ 18.5 min). This value is of the same order of magnitude to the first seiche mode period of 15 min, considering the first seiche mode period as $\frac{4L}{\sqrt{gh}}$ with L= 500 m, the width of the reef, and h= 0.5 m, the mean water depth. On the reef flat, the level of IG and VLF energy is higher during extreme events (Fig. 3c) suggesting that the GW energy is the forcing mechanism. As a result of the high proportion of wave energy in the GW range at the RS, the energy in the VLF and IG are comparatively dwarfed (cf. Fig. 3b). Contrary to appearances, the energy at the RF and RS in the VLF and IG ranges remain comparable, with a factor 1.5 between RF and RS H_{IG} (cf. Sect. 4.2.1).

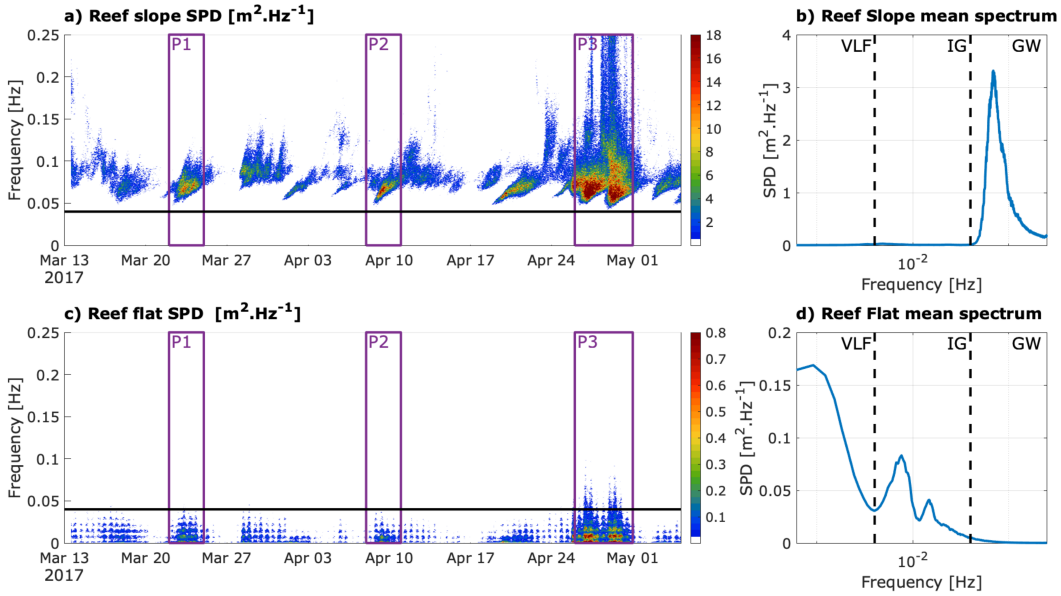

Figure 3. Wave energy spectrum: Temporal evolution at the RS station (a) and at the RF station (c), Total mean wave spectrum over the 53-days of experiment at RS station (b) and at the RF station (d). The black lines represent the frequency bands boundaries (0.04 Hz for IG/GW bands and 0.004 Hz for VLF/IG bands) Periods P1, P2 and P3, corresponding to the wave events of interest, are highlighted by the purple boxes.

4.2 Wave and water level observations

4.2.1 Water levels

Figure 4 shows the time series of the water level and wave parameters measured at the reef slope and reef flat stations. The observed tide was similar to the one described in Fig. 3a, mainly semi-diurnal with a diurnal inequality, covering two neap tides and two spring tides. The tidal range was almost similar in the reef slope and in the reef flat, around 0.5 m for the two spring tides and 0.2 m for the two neap tides. The maximum high tide was +0.23 m and the minimum low tide -0.24 m for the first spring tide, respectively +0.19 m and -0.35 m for the second spring tide. For the first neap tide, the maximum high and minimum low tides were 0.08 m above and below datum respectively, for the second neap tides the maximum was +0.01 m and the minimum was -0.20 m (Fig. 4a).

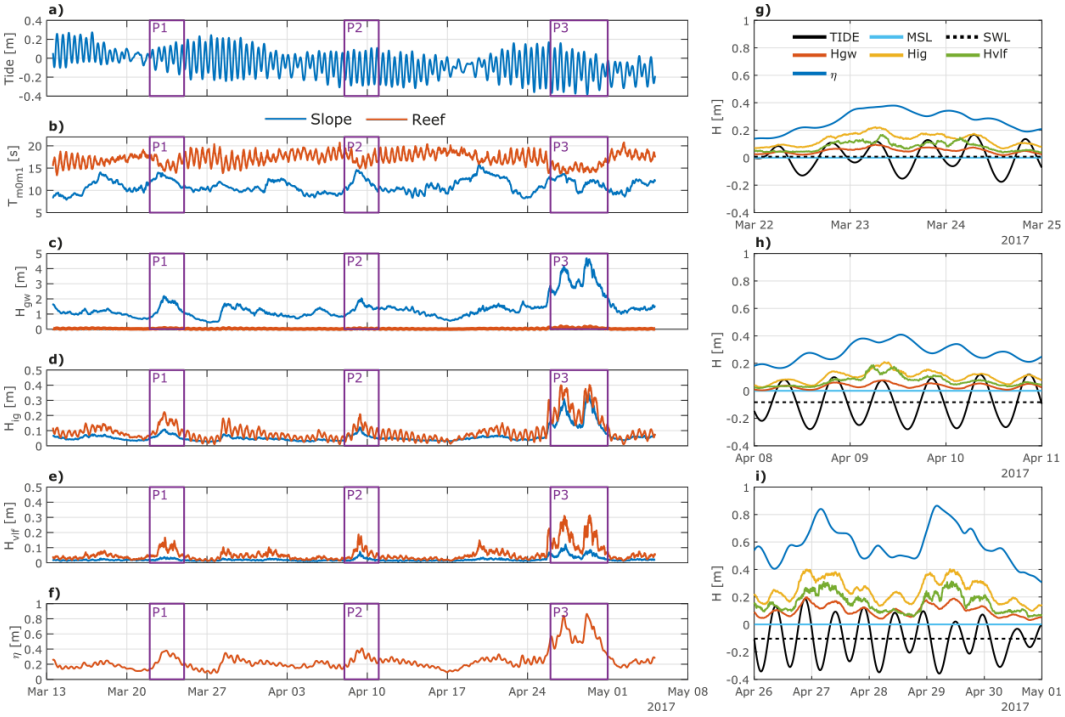

Figure 4. Overview of hydrodynamic measurements. On the left hand side, the water levels and wave parameters for the reef slope (in blue) and the reef flat (in red) observations over the 53-days of deployment: (a) Tide (relative to IGN89 datum) (b) Mean spectral period. (c-e) Significant wave heights in the GW band H_{GW}, IG band H_{IG}, and VLF band H_{VLF}. (f) Setup η computed at the RF station. On the right hand side, zoom on: (g) P1, (h) P2 and (i) P3 periods for the reef flat parameters. Each zoom is illustrated with the tide (black line), the level of reference (blue horizontal line at 0 m), the still water level (SWL, black dotted line), as well as H_{GW}, H_{IG}, H_{VLF}, and setup (shown with orange, yellow, green and blue curves, respectively).

4.2.2 Short and long waves in the reef

The reef slope GW significant wave height H_{GW}^{RS} was 1.4 m on average, with mean and maximum spectral energetic period $T_{m0,-1}$ of 10.9 s and 15.8 s respectively (Fig. 4b and 4c). For the two swell events of the periods P1 and P2, H_{GW}^{RS} reached $\approx$ 2 m with periods $T_{m0,-1}$ = 13.9 s during P1 and 14.5 s during P2. The stronger swell event P3 that occurred at the end of April was a double peaked swells with a first event H_{GW}^{RS} = 4.2 m and $T_{m0,-1}$ = 13.6 s, and a second event characterized by higher wave heights (H_{GW}^{RS} = 4.7 m) and lower periods ($T_{m0,-1}$ = 11.7 s). In the reef flat, during P1 and P2 events, the significant GW heights did not exceed 10 cm, but reached 20 cm during P3, demonstrating the marked attenuation of short wave components by the reef. This GW attenuation across the reef flat is evident with a 97% mean reduction of the incident wave heights (Fig. 5a), and an observed H_{GW}^{RS} of 0.04 m on average (cf. Fig. 4c). Wave attenuation varied between 92% and 98% from high tide to low tide respectively, suggesting that the tidal fluctuations partially controlled the gravity wave energy reduction, with a lower attenuation of incident waves during high tide, and greater attenuation during low tide (Fig. 5a).

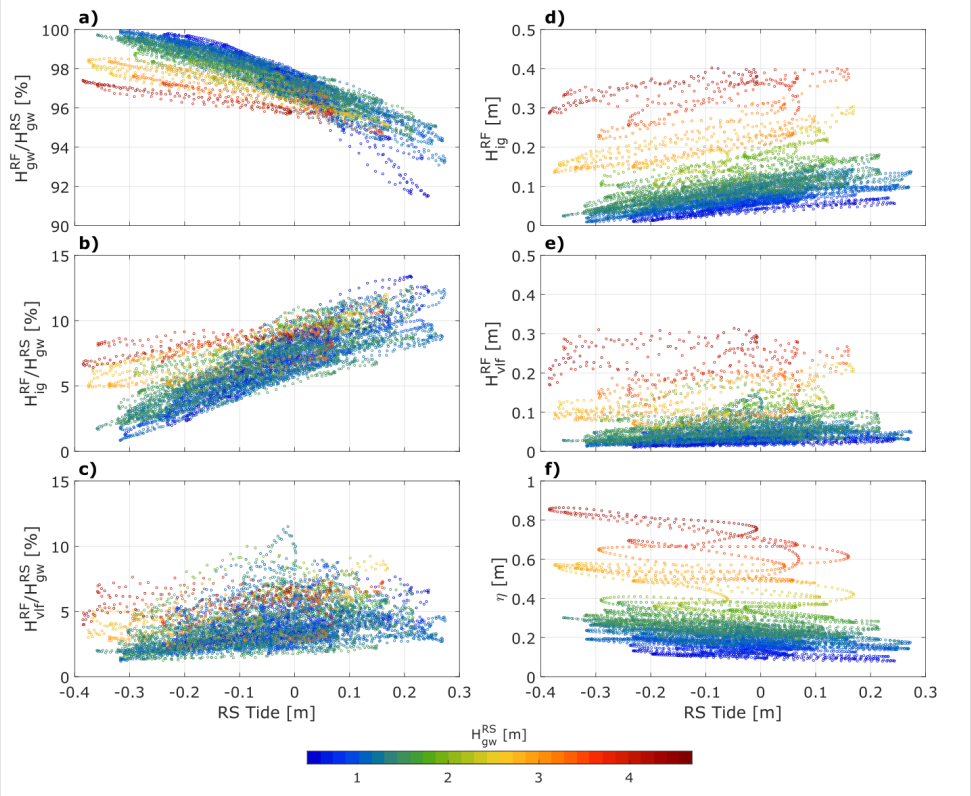

Figure 5. Tidal control on wave processes in the RF: (a) GW attenuation, (b-c) ratio between the low frequency waves (IG and VLF) of the RF and RS GW, (d-e) IG and VLF wave heights, (f) setup at RF station. All scatter plots are coloured by the height of the reef slope gravity waves.

The transformation of the waves while they propagate across the reef is clearly evident with spectral analysis (Fig. 3) through the filtering of the high-frequency, related to the dissipation of the shorter frequencies due to breaking and bottom friction and an energy transfer to lower frequencies. On the reef flat observations, the simultaneous increase of the lower frequency wave heights and decrease of the gravity waves confirmed this process (Fig. 4d–e, 4g–i). Over the entire studied period, the synchronicity between the long wave variability on the reef flat (IG and VLF wave heights in Fig. 4d–e) and the reef slope gravity waves (Fig. 4c), suggests that the lower frequency waves that appeared in the reef flat were primarily controlled by the incident swells.

The IG wave heights in the reef flat ranged from 1% to 12% of the incident oceanic gravity wave conditions (Fig. 5b) and were on average 1.5 times greater than the infragravity waves observed on the reef slope (H_{IG}^{RF}=9.4 cm and H_{IG}^{RS}=6.2 cm). This ratio was clearly modulated by tide, increasing with the water level on the reef, but this tidal modulation behaved differently above an incident GW height threshold H_{GW}^{RS}=2.5 m and was reduced to a quasi-constant ratio value (Fig. 5b), suggesting that the reef flat infragravity waves became primarily controlled by incident short waves rather than tides. The tidal modulation of the reef flat IG wave heights is also evidenced by an oscillating component of these IG waves in phase with tidal signal (Figs. 4g-i), increasing with the rising tide (Fig. 5d). While focusing on the 3 periods of interest, for which the mean tidal range increases from P1 to P3 (see Table 1), the amplitude of the tidal modulation appeared more pronounced for stronger tidal range (Figs. 4g-i). The amplitude of IG wave reaches up to 40 cm during P3.

Similarly, very low frequency wave heights on the reef flat were enhanced by a factor of 2.6 on average, between the reef slope and the reef flat, corresponding to mean wave height H_{VLF}^{RF}=5.6 cm on the reef flat and H_{VLF}^{RS}=2.1 cm on the reef slope. The ratio between VLF wave height in the reef flat and gravity waves on the reef slope ranged from 1% to 10% (4% on average) with very slight modulations at a tidal scale, less pronounced during energetic events (Figs. 4g–i and Figs. 5c, 5e). During P3, VLF significant wave height reaches 30 cm.

4.2.3 Wave friction factor estimation on the reef

In order to reproduce the variability of the gravity waves on the reef flat H_{GW}^{RF}, wave dissipation due to breaking and the bottom wave friction must be considered. We used the analytic expression for the wave height decay onshore of the surf zone (Lentz et al., 2016), assuming a constant water depth, the wave friction factor f_w and shallow water waves (Eq. 6):

$$H_{GW}^{RF}(L) = \gamma \frac{D+\eta}{1+\frac{L}{L_d}} \tag{6}$$

In this equation, L is the distance separating the measurement location and the reef crest, D is the water depth and η the setup, γ is the breaker index equal to the wave height to water depth ratio at the onshore edge of the surf zone, and $L_d = 8\sqrt{2\pi}\frac{D+\eta}{\gamma f_w}$ is a frictional decay scale in which f_w is the wave friction factor. Note that in this equation, in absence of frictional wave dissipation ($f_w = 0$ the wave height is directly related to the water depth by the breaker index as expected $H_{GW} = \gamma(D+\eta)$).

To accurately reproduce the dependence of wave height on water depth in the reef flat, the two parameters f_w and γ must be correctly chosen. In absence of observations in the breaking zone to quantify wave height and water depth, the breaker index was set to $\gamma = 0.55$ equal to the default value used in the XBeach model (see Sect. 3.2 on model configuration). The wave height variability described by Equ. 6 is well-reproduced for a wave friction parameter f_w=0.2 (see the red curve on Fig. 6), reinforcing the assumption that the bottom friction plays a key role in the relationship between wave height and water depth on the reef flat after the breaking zone. When bottom drag dissipation is large, the ratio H_S/D is not representative of the value of the ratio γ in the surf zone, illustrated by the black dashed line in Fig. 6.

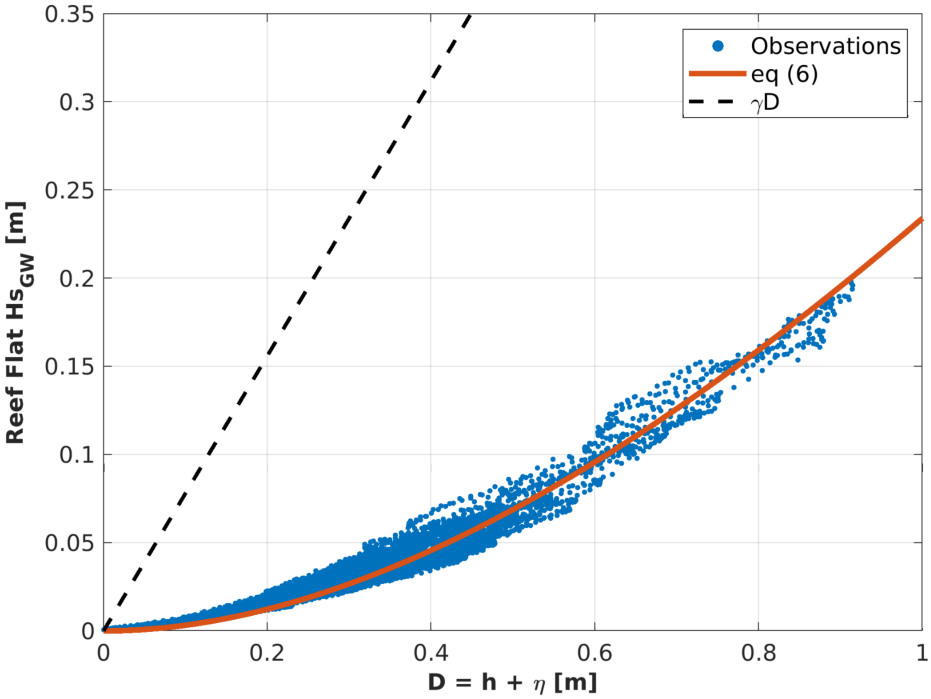

Figure 6. GW height at RF station according to the modified depth above the reef crest following the adapted Lentz et al. (2016) equation (Eq. 6).

4.2.4 Setup

Wave setup on the reef ranged from 0.08 m (12% of incident H_{GW}) to 0.86 m (18% of H_{GW}) with a mean value of 0.25 m, representing 18% of the incident offshore mean wave height. Considering the strong correlation coefficient obtained for Eq. (2) (R^2= 0.95), the setup in the reef is highly correlated to the incident wave height. Meanwhile, for similar incident conditions, the setup is slightly lower at high tide and higher at low tide (Fig. 5f). The setup variations are in antiphase with the tidal signal (blue curve in Fig. 4g-i). The maximum observed setup is 0.86 m during the extreme event P3 corresponding to incident wave height H_{GW} = 4.7 m and energetic period $T_{m0,-1}$ = 11.7 s and a tide level -0.36 m relative to IGN89 datum. Similarly to IG and VLF waves, setup increases more rapidly for incident waves above 2.5 m in significant wave height.

4.3 Model results

4.3.1 Model validation

A comparison of the measured and modeled wave characteristics across the fringing reef is presented in Fig. 7. Strong correlations indicate that the model configuration used in the present study is well adapted for predicting H_{GW}, H_{IG} and setup over the reef.

Since the model was forced by wave spectra issued from the offshore records, it is not surprising to find a good correlation for the gravity waves on the reef slope (H_{GW}^{RS}) with R^2=0.99 (Fig. 7a). However, modeled wave heights seemed to be slightly underestimated for the strong swell event P3 (Fig. 7f).

The performance of the model was good in the reef flat with $R^2 > 0.88$, bias < 0.033 m and $RMSE < 0.046$ m based on the output H_{GW}^{RF}, H_{IG}^{RF}, and setup on the reef flat (Figs. 7b, 7c and 7e). The gravity waves in the reef flat were well-represented during the P1 period, but overestimated for P2 and P3 periods for observed $H_{GW}^{RF} < 0.12$ m in the reef flat and underestimated for $H_{GW}^{RF} > 0.12$ m (Fig. 7g). Despite good performance metrics of the model for IG waves in the reef flat, they were generally underestimated during the 3 periods of interest (Fig. 7h). The model behaved especially well for the prediction of the setup with a slight underestimation in the reef flat for values greater than 0.4 m during the P3 period (Fig. 7j).

The VLF wave heights on the other hand were poorly replicated by the model with a weak R^2=0.41 for the whole period, and clearly underestimated over the 3 periods of interest, but their variability is numerically captured overall, with the exception of P3 (cf. Fig. 7d).

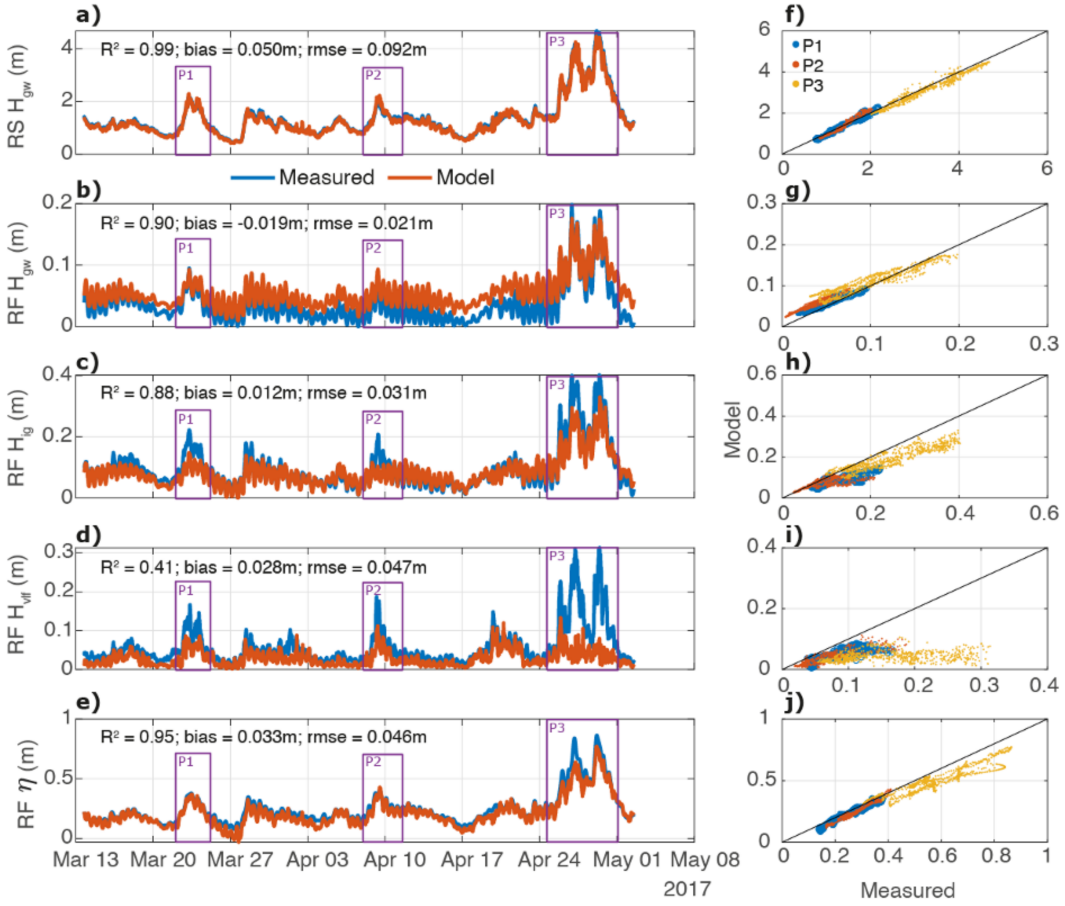

Figure 7. Comparison of measured and modeled reef hydrodynamics. Left hand side panels: timeseries of the modeled (in red) and observed (in blue) wave parameters on (a) the reef slope, (b–d) the reef flat and (e) setup on the reef flat. The performance metrics of the model over the whole period that are R^2, the *Bias* and the *RMSE*, are also indicated. Right hand side panels: scatter plots of measured vs. modeled parameters for the 3 periods of interest, P1 in blue, P2 in red and P3 in yellow.

4.3.2 Modeled setup and runup

Figures 7e and 8 show that the XBeach model performs very well for the prediction of the setup for the P1 and P2 periods. The setup increases with the H_{GW} at the reef slope and the tidal control on the setup is well reproduced (Fig. 8b). For the P3 period, the bias between the measured and the modeled setup increases and reaches 10 cm. The modeled runup is globally 10 cm above the setup during P1 and P2, and is extreme during the P3 period, reaching 1 m, whereas the simulated setup is slightly underestimated. During this period, the simulated runup increases up to 40 cm above the simulated setup during the first energy peak of the P3 event (Fig. 8c).

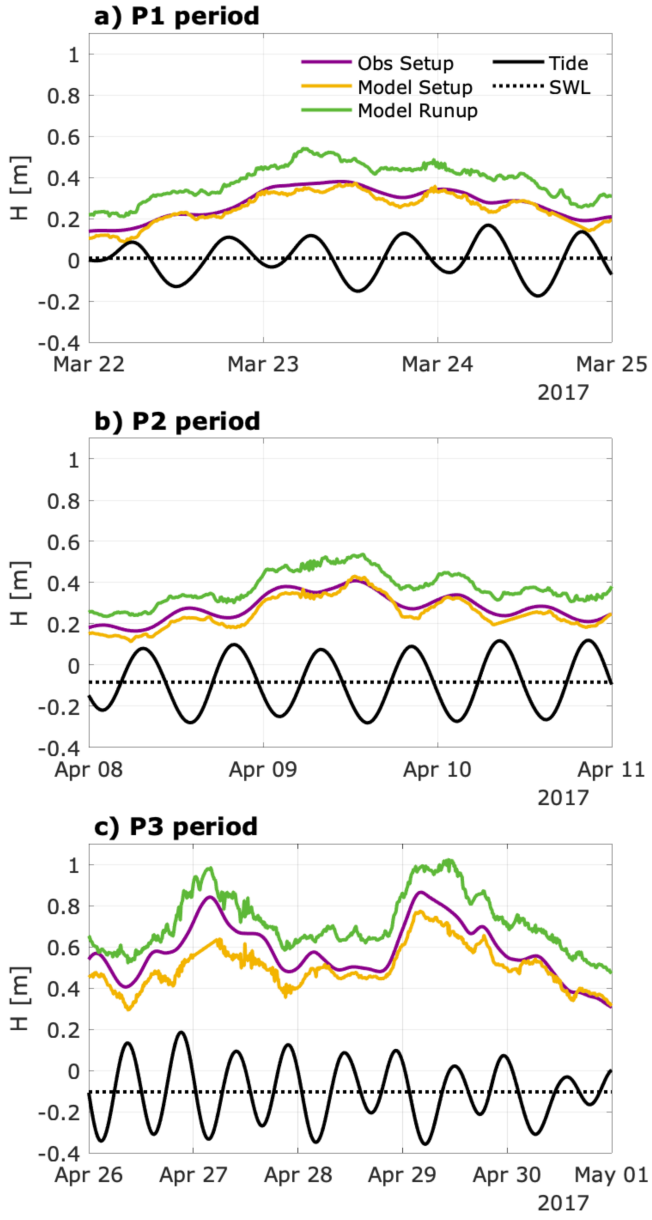

Figure 8. Observed and simulated levels during a) P1, b) P2 and c) P3 events: setup height (m) over the reef flat computed from observations (purple line), modeled setup (yellow line), modeled wave runup at the beach (green line), observed tide (black line) and still water level (dashed black line).

The relative contributions of the other water level parameters composing the runup are also investigated (Fig. 9). The offshore tide level is shown to contribute to about 19% over the whole period, and also during extreme events. The setup contributes to the most important part of the runup, by approximately 68% for the whole period, 67% for P1 and

P2, and 61% for P3. The main differences lie in the contribution of the gravity waves on the reef flat, which contribute to 1% of the runup for the P1 and P2 events, and more than 7% during the P3 event. The longer waves (IG and VLF) equally explain 5% to 7% of the runup for all the periods, with an exception of the IG waves which account for 10% of the runup during the P1 period. The relative importance of each variable in the runup reinforces the assessment that each of these parameters must therefore be correctly predicted according to offshore water level and energy in order to correctly quantify the evolution and variability of the runup.

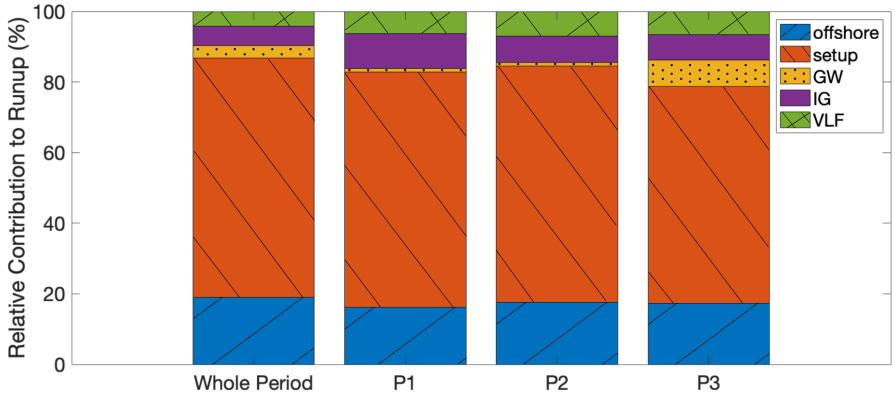

Figure 9. Relative contributions of tide (offshore level), setup, GW, IG and VLF at RF station to Runup during: (from Left to Right) the whole period, P1, P2 and P3.

4.4 Transfer functions

Transfer functions (using multiple linear regressions) are fitted between incident conditions (offshore water level and wave parameters) and reef flat parameters (H_{GW}, H_{IG}, H_{VLF}, setup and runup) in order to be able to predict the runup in the context of global change. Several parameters are considered: the offshore water level relative to the reef crest D, the distance to the reef crest L, the GW significant wave height and period at the RS station, wave energy, wave power, or even $H_S T_m^2$ (Ardhuin et al., 2014). The best fits and correlation statistics are presented in Fig. 10 and Table 2. Figure 10 highlights the dependency of RS H_{VLF}^{RS} and H_{IG}^{RS} to the incident wave power ($R^2 = 0.83$ and 0.97 respectively) and of the RF H_{VLF}^{RF} and H_{IG}^{RF} to significant wave height, water level and incident wave power (R^2= 0.85 and 0.95 respectively). The statistical parameters and best fit equations are summarized in Table 2, considering $P = H_{GW}^2 \times T_{m0,-1}$. These transfer functions highlight the fact that the forcing mechanism is oceanic swell. The water level at the RF is shown to positively influence the H_{VLF} and H_{IG} by 4 and 12% (Table 2).

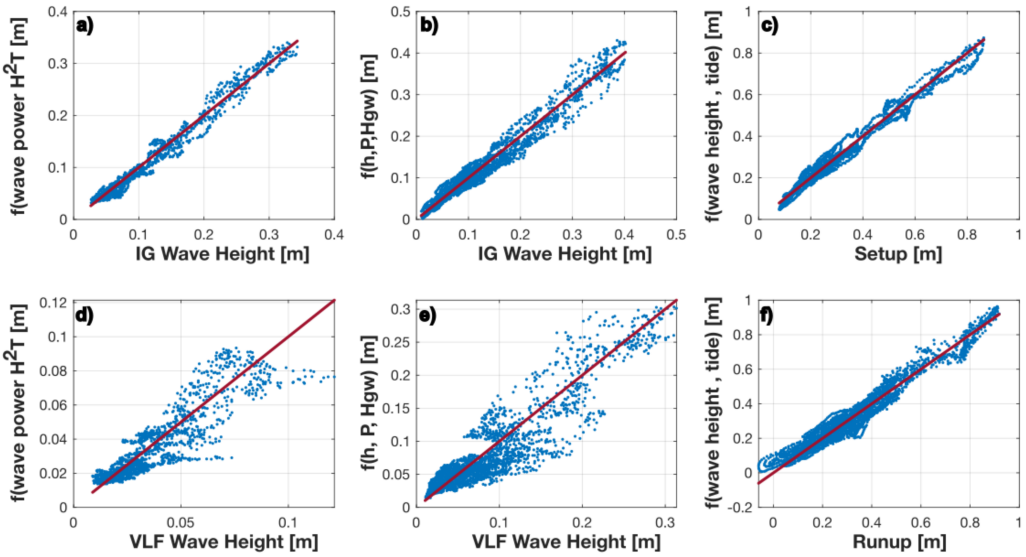

Figure 10. Best fit functions, as presented in Table 2, for the prediction of (a) RS IG wave height, (b) RF IG wave height, (c) Setup, (d) RS VLF wave height, (e) RF VLF wave height, and (f) Runup. Red lines represent identity. Correlation statistics for the above relations are presented in Table 2.

Table 2. Transfer function, best fit function according to multilinear regression, for 6 variables (see Fig. 10) with the associated R^2, $RMSE$ and the ratio of explained variability by each individual parameter.

Parameter	Transfer Function	R^2	$RMSE$	Predicted %var		
				RS Tide	RS H_{GW}	RS P
H_{IG}^{RS}	$0.0012P + 0.03$ (7)	0.97	0.9 cm	-	-	99.9%
H_{VLF}^{RS}	$0.0003P + 0.013$ (8)	0.83	0.6 cm	-	-	99.9%
H_{IG}^{RF}	$0.187h + 0.045\ H_{GW} + 0.0009P + 0.021$ (9)	0.95	1.5 cm	12%	86%	2%
H_{VLF}^{RF}	$0.07h + 0.004\ H_{GW} + 0.001P + 0.026$ (10)	0.85	1.9 cm	4%	89%	7%
RF Setup	$0.176\ H_{GW}$ - $0.144h$ (11)	0.97	2.3 cm	2%	98%	-
RF Runup	$0.210H_{GW} + 0.593h + 0.041$ (12)	0.94	4.1 cm	21%	79%	-

A transfer function reaching R^2=0.97 with a standard deviation of 2 cm is found for the setup using the RS GW height and the water level (Table 2 and Fig. 10c). 98% of setup is explained by incident wave conditions. The water level negatively influences the setup and is responsible for 2% of its variability. Furthermore, 79% of the runup is explained by incident wave conditions and 21% by tidal fluctuations. Combining both forcings leads to

R^2=0.94 with a RMSE of 4 cm (Fig. 10f and Table 2). The higher the offshore water level, higher the runup at the shoreline.

5 Discussion

The objective of this study is to provide a better understanding of the coastal defense capabilities of the fringing La Saline reef system at la Réunion Island, as a function of the incident wave field and tidal characteristics. Field data was collected to study incident wave spectra over a 53 day period, during which the study site was exposed to a range of energetic swell events generated in the Southern Ocean. These field observations were used to calibrate the XBeach numerical model, allowing an investigation of wave transformation processes as well as setup and runup in the reef system.

5.1 Gravity wave driven hydrodynamics

A first step in the study was to perform an inventory of the hydrodynamic components in the study area. Pressure sensor measurements show the presence of gravity waves, infragravity waves, and very low frequency waves on the reef flat, as previously reported in similar environments (e.g., Bonneton et al. (2007); Ferrario et al. (2014); van Dongeren et al. (2017); Pearson et al. (2017)). The study of IG and VLF wave magnitudes demonstrates that the lower frequency components observed at the reef slope and reef flat are strongly in phase with incident GW swell conditions (Figs. 4, 5, 7 and Table 2), confirming that waves sourced from the open ocean are the main driver of the reef system hydrodynamics. This is in line with similar findings at other reefs (e.g., Beetham et al. (2016)).

5.2 Wave dissipation

Coral reefs offer substantial protection against natural hazards (e.g., Ferrario et al. (2014); van Dongeren et al. (2017)). The coastal defense abilities of La Saline fringing reef are first confirmed by the average reduction of 97% of GW energy over the whole measurement period. While most of the energy reduction occurs at the reef crest (Vetter et al., 2010; Ferrario et al., 2014; Monismith et al., 2015), bottom friction contributes to wave dissipation of waves propagating over the reef flat canopy (Symonds et al., 1995). This friction factor f_w varies considerably between study sites, ranging from 0.1 to 1 (Lowe et al., 2005; Rogers et al., 2016; Harris et al., 2018), reaching f_w =1.8 for extremely rough reefs (Monismith et al., 2015) or f_w =5 on a platform coral reef (Lentz et al., 2016).

To estimate f_w in La Saline reef, we first use the depth-dependent analytical model (cf. Equ. 6) introduced by Lentz et al. (2016) for fringing reefs. The best fit of this formulation to our field measurements is found for an average value of f_w=0.2 (cf. Fig. 6) for the entirety of the campaign, considering a breaker index $\gamma = 0.55$ similar to the default value in the XBeach model. This inferred friction factor is within the range of values reported by authors such as 0.3 at the Kanehoe barrier reef (Lowe et al., 2005), and 0.2 at Moorea's north shore fringing reef (Monismith et al., 2013). Still, f_w=0.2 is a relatively low friction factor for coral reefs. With such a value, our study demonstrates that this friction factor leads to a wave decay close to 40% more intense than when considering wave breaking only (compare black line and red line for a fixed water level value in Fig. 6). Such results are dependent on factors such a reef health and water level, which are both expected to evolve with predicted environmental change (IPCC report, Hoegh-Guldberg et al. (2014)).

As seen on Figure 6, the analytical model (Lentz et al., 2016) is validated in the case of the La Saline fringing reef. These results illustrate the importance of bottom friction and of water level on the wave decay across the reef flat. Indeed, higher water levels lead to reduced dissipation due to wave breaking and bed friction dissipation (e.g. Fig. 5a). We note that in the case of the platform coral reef configuration studied by Lentz et al. (2016), it is not clear if setup plays a major role in GW height over the reef flat. We highlight that

over a fringing reef such as La Saline, the setup, of a few dozen centimeters, is of the same order of magnitude as the water depth below the still water level (Figs. 4 & 8). Setup is an essential and even dominant component in calculations of wave dissipation (cf. Fig. 9). As setup over the reef flat decreases, so does the bed friction dissipation as the total water depth is increased. As it becomes clear that the total water depth on the reef flat (including the setup) must be reported at the breaking location (at the reef crest), the correction (by subtraction) of the generally higher level found at the reef crest is necessary, with the aim of attaining $D = 0$ in conditions of absent waves at the reef crest (H_{GW} at RF station). Whereas in (Lentz et al., 2016), much data was in the linear part of the model (cf. Equ. 6), the present study completes the validation, by adding much data in the polynomial section of the curve, at low water levels (cf. Fig. 6).

5.3 Wave transformation

As the gravity wave components are dissipated over the reef, lower frequency waves are amplified (i.e., infragravty (IG) and very low frequency (VLF) waves). Pressure sensor data show that IG and VLF components represent 7% and 4% of the total incident wave energy, but experience an average 150% increase in H_{IG}, and a 260% increase in H_{VLF} over the reef flat. These observations demonstrate the low-pass filtering capacity of the reef, already evidenced in a number of field, laboratory and modelling experiments (A. Pomeroy et al., 2012; Van Dongeren et al., 2013; Péquignet et al., 2014; A. W. Pomeroy et al., 2015; Beetham et al., 2016; Cheriton et al., 2016). For the lower frequency wave components, we find that VLF and IG waves height at the RS station are linearly related to incident wave power (Fig. 10 and Table 2). In addition to being strongly related to wave height (86% of variance explained by offshore wave heights, cf. Table 2), IG wave height on the reef flat is also strongly modulated by the water level (12% of variance explained, Table 2). Since the breaking is modulated by the depth, this would explain the influence of the depth on the IG wave height at RF station. Then, IG wave energy that is not dissipated over the reef flat may be reflected seaward, and might lead to resonant VLF waves (Gawehn et al., 2016; Bertin et al., 2018). This would explain the fact that the RF H_{VLF} and RF H_{IG} transfer functions show the same variability. In our study, the VLF waves have a mean period of 18 minutes, and the first seiche mode predicted according to the geometric configuration of our study site is 15 minutes. However, the expected variation of the VLF waves' mean period with the water depth is not observed. The presence of double peaks in the IG range reflects possible harmonic behavior, which remains to be investigated (Sous et al., 2019).

5.4 Model validation and predicted runup

A second step of this study was to predict wave runup and potential flood risk at the shoreline using an XBeach numerical model implemented and calibrated with field measurements at the RS and RF stations. Results show that with a friction coefficient $f_w = 0.3$ and a Manning formulation of with $n = 0.02$, the wave model was able to reproduce wave transformation processes correctly. This f_w value is close to the values obtained from the Lentz et al. (2016) formulation.

As shown in Figure 7, the XBeach model performs best for the reproduction of gravity wave dissipation over the reef ($R^2 = 0.90$ against the field data). For the infragravity waves, the model underestimates the higher H_{IG} values by approximately 25% relative to the field data. With this model configuration, the XBeach model is unable to correctly reproduce VLF amplification in the reef flat ($R^2 = 0.41$) observed from the field data. It is therefore possible that the transfer of energy to lower frequency bands or the reflection of the IG wave at the shore are not sufficiently reproduced to generate a resonant mechanism of the measured intensity. This could be explored using the short wave-resolving non-hydrostatic version of the XBeach model (e.g., Pearson et al. (2017); Scott et al. (2020)).

The weaker prediction of H_{VLF} by the model was initially attributed to the frequency at which new incident waves and tide are applied at the offshore boundary of the domain. During the first simulations, these forcings were applied at the boundary every 10 minutes, resulting in the too frequent reinitialization of the free surface for the full development of VLF waves. However, modifications to allow for a delay of 60 minutes or 180 minutes between each forcing do not improve VLF height prediction, only their periods. During these tests, noise in the surface height variations also increased with the increase in forcing delay. As a result, the 10 minute forcing intervals were kept for the present paper.

Though the incident conditions and the wave dissipation are well simulated, as well as the setup during mild conditions, an underestimation of the highest setup is observed, reaching 25% of the observed setup during the P3 extreme event (see Fig. 7j). Buckley et al. (2015) give a first possible explanation for the underprediction of the setup, using laboratory experiments. Results reveal that the use of linear wave theory to calculate the radiation stress gradients leads to underpredicted setup, especially for cases with larger wave heights and lower still water levels, corresponding with our P3 event (cf. Table 1). A second possible explanation of the error in predicted setup for strong offshore wave conditions could be explained by the absence of 3D current shear in the presented simulations to 3D current shear, despite inducing wave setup (Guérin et al., 2018), during intense during extreme events especially. Guérin et al. (2018) numerically show that for a 1:20 slope, the contribution of such vertical processes in the surf zone could lead to a 20% increase of the total setup, and this effect is expected to increase with beach slope (1:10 in the present study).

5.5 Setup and runup

The observed setup patterns are well reproduced by the model (Figs. 7 and 8). Setup is larger for higher offshore significant wave height and is also modulated by the water level, with a slight decrease of the setup at high tide and a slight increase at low tide as previously observed (Bonneton et al., 2007; Becker et al., 2014; Sous et al., 2020). A lower water level leads to more breaking at the reef crest and thus a bigger contribution to the setup. The transfer functions computed in this study also show that setup is largely forced by the breaking of gravity waves over the reef, predicting 98% of the variance of the setup in the reef, that is scaled at 18% of the reef slope wave height, thus ranging from 0 to 0.8 m for 0 to 4 m of incident wave height. The tide only contributes for 2% of the setup variability (Fig. 10c and Table 2). Vetter et al. (2010) also found setup to be highly correlated with incident wave heights in a shore-attached fringing reef with shallow depths over the reef flat and a steep fore reef. Their findings improve on previous attempts that have relied on the wave height and its product with wavelength to predict setup (e.g., Bonneton et al. (2007); Sous et al. (2020)).

Finally, the simulated runup is shown to be primarily driven by the setup (Fig. 9), and can be well-predicted in a transfer function using the offshore wave height and water level (R^2=0.94, Fig. 10f). This function show that 79% of the runup variability is explained by the incident wave conditions, scaled as 20% of incident wave height, and 21% is explained by the tide. Since setup is the main contributor to runup, and setup is shown to be underestimated for strong wave heights as the P3 event observed during the present study, the maximum runup computed that is around 1 m (Fig. 8c), might therefore be underestimated as well. Thus, even if the offshore GW energy is highly dissipated and incident GW heights are clearly reduced on the reef flat, our results show that strong setup and runup (about 1 m for 4m wave height) can be expected in the fringing reef of La Saline and the adjacent shoreline. Such setup and runup increase have already been evidenced and supposed to be enhanced for steep reef environments (Becker et al., 2014; Buckley et al., 2015; Gawehn et al., 2016; Pearson et al., 2017; A. C. N. Péquignet et al., 2009; Quataert et al., 2015). The occurrence of large wave height to water depth ratios at the breakpoint, similar to the conditions observed during the P3 event of this study, results in larger radiation stress

gradients in shallow water and the transfer of kinetic energy into even shallower water. This may enhance setup on steep fore reef slopes (Buckley et al., 2015). IG waves at the shore can be reflected and then trapped on the reef flat if outgoing low-frequency waves are reflected again at the reef crest. This process depends on the reef geometry and can result in resonant amplification of wave motions that may enhance runup (e.g. Gawehn et al. (2016); Pearson et al. (2017).

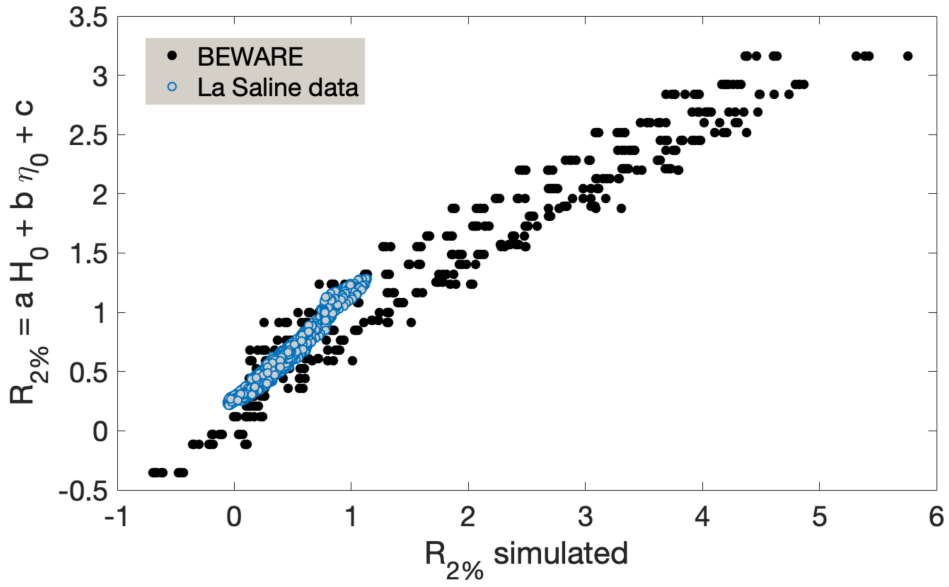

Figure 11. Comparison of the simulated runup from the presented configuration of this study and from BEWARE (Pearson et al., 2017) to the transfer function calibrated in this study (Eq. 12, Table 2). The BEWARE data points correspond to an idealized bathymetry with 500m reef width, $c_f = 0.05$, a 1/20 reef slope and a 1/10 beach slope.

5.6 Implications for stake-holders

The present study produces reliable empirical formulations in order to predict low frequency wave height (IG and VLF), setup, and runup on a reef flat according to offshore observations of the incident significant wave height and water level fluctuations. These two offshore variables can be easily retrieved via open-access datasets. The offshore wave heights can be downloaded at a regional scale from the WaveWatch III numerical model or at a local scale from the French National Network CANDHIS (http://candhis.cetmef.developpement-durable.gouv) which operates a nearshore wave buoy and provides public access to real time and archived data (see Fig. 1 for the localization of these two points of accessible data). In a similar way, the offshore tide can be retrieved through public access at Hydrographical Service of French Marine Shom website (www.data.shom.fr).

The runup formulation derived here (Equ. 12) is the most relevant outcome for the civil society and stakeholders because it enables the fast, reliable prediction of nearshore water levels for coastal flood risk assessments. In this study, the transfer functions are calibrated for significant wave heights reaching 4.5 m at the reef slope during SSW Southern Ocean swell, and water depths above the reef crest comprised between up to 1.5 m, covering a wide range of marine meteorological conditions.

Several previous studies have developed tools for use in early warning systems or risk assessment, or to make projections about how wave-induced flooding on coral reef-lined coasts may change as a result of climate change (e.g., Rueda et al. (2019); Scott et al. (2020)). Such tools may provide a useful basis for comparison with the results from our study. For example, Pearson et al. (2017) developed BEWARE ("Bayesian Estimator for Wave Attack in Reef Environments"), a large synthetic reef hydrodynamics database created with the same process-based hydrodynamics model used in the present study, XBeach, but in wave-resolving mode (XBeach Non-Hydrostatic,"XBNH"). To construct this database, Pearson et al. (2017) used idealized bathymetry and reef morphologies, commonly encountered in the nature. When comparing their results for similar reef geometry to the one of La Saline fringing reef, i.e. an idealized bathymetry with a 500 m reef width, a 1:20 reef slope and a 1:10 beach slope, a coefficient of friction $c_f = 0.05$, our predictions derived using equation 12 match well for low runup (Fig. 11). This raises the question of whether taking account of the full architectural complexity of a fringing coral reef is completely necessary. Even if a number of studies (e.g. Van Dongeren et al. (2013); Quataert et al. (2015); Lentz et al. (2016); Harris et al. (2018)) suggest that local studies are necessary in order to consider the real reef structural complexity, specific to each reef, our results compared to the results issued from the database of Pearson et al. (2017) suggest that idealized configurations of reef systems with good friction parameterization should be enough to reproduce the water level in the reef flat (setup) or at the shore (runup). The present study lies in the low range of runup values studied in BEWARE (only 1 m in Fig. 11), but similar comparisons could be conducted for stronger runup if measurements become available in the future.

Even if La Saline is in a microtidal environment, the geometric configuration of reefs with a shallow reef crest leads to an enhanced influence of the water level. The water level modulates the breaking and the bed dissipation. For the moment, the water level oscillates close to the reef crest, since the coral has grown and kept pace with the sea level rise to date. However, under accelerated sea level rise scenarios, the coral may not be able to grow fast enough to keep up. As a consequence, the water depth above the crest will increase, breaking fewer waves and permitting more gravity waves to cross the reef flat (Fig. 5), leading to potentially higher runup (Fig. 8, P3) and greater flooding.

The potential impact of climate change can also be considered by adopting a median sea level rise of 50 cm (projected for 2081-2100 according to the scenario RCP4.5 with moderate emission trajectories (IPCC report, Hoegh-Guldberg et al. (2014)). A 50 cm increase in mean water depth at the reef flat D would result in a mean increase of wave heights and runup in the reef system, such as a reef flat signficant wave height $H_{GW}^{RF} = 50$ cm for 4 m offshore significant wave height. Furthermore, the setup over the reef flat, which is expected to decrease as D decreases, could become less dominant in the La Saline reef hydrodynamics. Extrapolating from the proposed transfer functions (cf. Table 2) infragravity significant wave height would increase by 9 cm, and beach runup by 30 cm. In the case of an event similar to P3, this will lead to an added runup of 1.26 m, thus enhancing sediment erosion and the likelihood of flooding inland. Moreover, the possible decrease in the coral cover and complexity with climate change (Hoegh-Guldberg et al., 2014; Camp et al., 2018; Harris et al., 2018) could induce a decrease of the reef's friction factor, which is shown to decay the wave height more than twice the wave decay induced by the wave breaking only (considering only $\gamma = 0.55$ instead of analytical model, Eq. 6). The resulting reduction of friction over the reef could accentuate the wave height increase, the runup increase, and the setup decrease in the reef system resulting from mean water level increase.

6 Conclusion

The present paper reports on a two-month long field experiment at La Saline fringing reef, La Réunion, France. The instrumentation was deployed along a single cross-shore transect to study wave transformation from the forereef to the inner lagoon. In addition, a series of numerical simulations were performed to further explain the field observations.

The study reveals strong swell wave attenuation across the fringing reef combined with significant energy transfer toward lower frequencies in the infragravity (IG) and very low frequency (VLF) bands. As a result of the strong gravity wave energy dissipation, the reef hydrodynamics are dominated by setup, reaching 0.86 m (18% of incident significant wave height at the reef slope). The swell transformation is well reproduced by the XBeach surf beat model, although further work is needed on the representation of VLF wave dynamics during extreme conditions over the reef flat. The observed VLF period ($\approx$ 18 min) may be attributed to partial reflection at the shore (quarter-wavelength case). Furthermore, in the absence of runup observations for comparison with model results, we think that a possible underestimation of runup during extreme energy conditions may occur as a result of the so-far neglected influence of current shear in the surf zone. We use an analytical expression to accurately describe the wave decay across the reef flat, which highlights the strong dissipation due to bottom friction. The present study demonstrates the ability of transfer functions to linearly combine water level and incident waves characteristics for predictions of reef flat hydrodynamics, notably setup and runup. Using the above results, we are able to speculate on the influence of sea level rise on hydrodynamics. For unchanging bed friction (reef health and composition), we predict a runup increase with increasing sea level. Future study should focus on the observation of wave runup for the understanding of underlying processes and numerical model validation.

7 Open Research

Data archiving for this study is currently underway. Data will be publicly available at https://geosur.osureunion.fr/.

Acknowledgments

This work was supported by CALHYCO and RenovRISK research programs, as well as the Geosciences Ocean lab (UMR6538), the Geosciences Laboratory of La Reunion (UMR 7154), LabexMER (ANR-10-LABX-19), the ISblue project (Interdisciplinary graduate school for the blue planet - ANR-17-EURE-0015), and was co-funded by the council of La Réunion Island and a "Investissements d'Avenir" French government grant.

References

Ardhuin, F., Rawat, A., & Aucan, J. (2014). A numerical model for free infragravity waves: Definition and validation at regional and global scales. *Ocean Modelling*, *77*, 20–32.

Baldock, T. E., Karampour, H., Sleep, R., Vyltla, A., Albermani, F., Golshani, A., ... Mumby, P. J. (2014). Resilience of branching and massive corals to wave loading under sea level rise - A coupled computational fluid dynamics-structural analysis. *Mar. Pollut. Bull.*, *86*(1-2), 91–101. doi: 10.1016/j.marpolbul.2014.07.038

Baumann, J. H., Ries, J. B., Rippe, J. P., Courtney, T. A., Aichelman, H. E., Westfield, I., & Castillo, K. D. (2019). Nearshore coral growth declining on the mesoamerican barrier reef system. *Global Change Biology*, *25*(11), 3932–3945.

Becker, J. M., Merrifield, M. A., & Ford, M. (2014). Water level effects on breaking wave setup for pacific island fringing reefs. *Journal of Geophysical Research: Oceans*, *119*(2), 914–932.

Beetham, E., & Kench, P. (2018). Predicting wave overtopping thresholds on coral reef-island shorelines with future sea-level rise. *Nature communications*, *9*(1), 1–8.

Beetham, E., Kench, P. S., O'Callaghan, J., & Popinet, S. (2016). Wave transformation and shoreline water level on Funafuti atoll, t uvalu. *Journal of Geophysical Research: Oceans*, *121*(1), 311–326.

Bertin, X., De Bakker, A., Van Dongeren, A., Coco, G., André, G., Ardhuin, F., ... others (2018). Infragravity waves: From driving mechanisms to impacts. *Earth-Science Reviews*, *177*, 774–799.

Bishop, C. T., & Donelan, M. A. (1987). Measuring waves with pressure transducers. *Coastal Engineering*, *11*(4), 309–328.

Bonneton, P., Lefebvre, J.-P., Bretel, P., Ouillon, S., & Douillet, P. (2007). Tidal modulation of wave-setup and wave-induced currents on the aboré coral reef, new caledonia. *Journal of Coastal Research*, 762–766.

Brander, R. W., Kench, P. S., & Hart, D. (2004). Spatial and temporal variations in wave characteristics across a reef platform, warraber island, torres strait, australia. *Marine Geology*, *207*(1-4), 169–184.

Buckley, M. L., Lowe, R. J., Hansen, J. E., & Van Dongeren, A. R. (2015). Dynamics of wave setup over a steeply sloping fringing reef. *Journal of Physical Oceanography*, *45*(12), 3005–3023.

Camp, E. F., Schoepf, V., Mumby, P. J., Hardtke, L. A., Rodolfo-Metalpa, R., Smith, D. J., & Suggett, D. J. (2018). The future of coral reefs subject to rapid climate change: lessons from natural extreme environments. *Frontiers in Marine Science*, *5*, 4.

Cheriton, O. M., Storlazzi, C. D., & Rosenberger, K. J. (2016). Observations of wave transformation over a fringing coral reef and the importance of low-frequency waves and offshore water levels to runup, overwash, and coastal flooding. *Journal of Geophysical Research: Oceans*, *121*(5), 3121–3140.

Chevalier, C., Sous, D., Devenon, J.-L., Pagano, M., Rougier, G., & Blanchot, J. (2015). Impact of cross-reef water fluxes on lagoon dynamics: a simple parameterization for coral lagoon circulation model, with application to the ouano lagoon, new caledonia. *Ocean Dynamics*, *65*(11), 1509–1534.

Cordier, E., Lézé, J., & Join, J. L. (2013). Natural tidal processes modified by the existence of fringing reef on La Reunion Island (Western Indian Ocean): Impact on the relative sea level variations. *Continental Shelf Research*, *55*, 119–128.

Cordier, E., Poizot, E., & Méar, Y. (2012). Swell impact on reef sedimentary processes: A case study of the La Reunion fringing reef. *Sedimentology*, *59*, 2004–2023. doi: 10.1111/j.1365-3091.2012.01332.x

Davy, C., Barruol, G., Fontaine, F., & Cordier, E. (2016). Analyses of extreme swell events on La Réunion Island from microseismic noise. *Geophysical Journal International*, *207*(3), 1767–1782. doi: 10.1093/gji/ggw365

Ferrario, F., Beck, M. W., Storlazzi, C. D., Micheli, F., Shepard, C. C., & Airoldi, L. (2014). The effectiveness of coral reefs for coastal hazard risk reduction and adaptation. *Nature communications*, *5*(1), 1–9.

Gawehn, M., van Dongeren, A., van Rooijen, A., Storlazzi, C. D., Cheriton, O. M., & Reniers, A. (2016). Identification and classification of very low frequency waves on a coral reef flat. *Journal of Geophysical Research: Oceans*, *121*(10), 7560–7574. doi: 10.1002/2016JC011834

Gerritsen, F. (1980). Wave attenuation and wave set-up on a coastal reef. In *Coastal engineering 1980* (pp. 444–461).

Grady, A., Moore, L., Storlazzi, C. D., Elias, E., & Reidenbach, M. (2013). The influence of sea level rise and changes in fringing reef morphology on gradients in alongshore sediment transport. *Geophysical Research Letters*, *40*(12), 3096–3101.

Guérin, T., Bertin, X., Coulombier, T., & de Bakker, A. (2018). Impacts of wave-induced circulation in the surf zone on wave setup. *Ocean Modelling*, *123*, 86–97.

Harris, D. L., Rovere, A., Casella, E., Power, H., Canavesio, R., Collin, A., ... Parravicini, V. (2018). Coral reef structural complexity provides important coastal protection from waves under rising sea levels. *Science Advances*, *4*(2). doi: 10.1126/sciadv.aao4350

Hoegh-Guldberg, O., Cai, R., Poloczanska, E. S., Brewer, P. G., Sundby, S., Hilmi, K., ... others (2014). The ocean. *Climate Change 2014: Impacts, Adaptation, and Vulnerability, Part B: Regional Aspects, Chapter 30*.

Hoegh-Guldberg, O., Mumby, P. J., Hooten, A. J., Steneck, R. S., Greenfield, P., Gomez, E., ... Hatziolos, M. E. (2007). Coral reefs under rapid climate change and ocean acidification. *Science*, *318*(5857), 1737–1742. doi: 10.1126/science.1152509

Holthuijsen, L. H. (2010). *Waves in oceanic and coastal waters*. Cambridge university

press.

Hom-ma, M., Horikawa, K., & Komori, S. (1966). Response characteristics of underwater wave gauge. *Coastal Engineering in Japan*, *9*(1), 45-54. doi: 10.1080/05785634.1966.11924671

Hughes, T. P., Anderson, K. D., Connolly, S. R., Heron, S. F., Kerry, J. T., Lough, J. M., ... others (2018). Spatial and temporal patterns of mass bleaching of corals in the anthropocene. *Science*, *359*(6371), 80–83.

Hughes, T. P., Baird, A. H., Bellwood, D. R., Card, M., Connolly, S. R., Folke, C., ... Roughgarden, J. (2003). Climate change, human impacts, and the resilience of coral reefs. *Science (80-.).*, *301*(5635), 929–933. doi: 10.1126/science.1085046

Hughes, T. P., Kerry, J. T., Álvarez-Noriega, M., Álvarez-Romero, J. G., Anderson, K. D., Baird, A. H., ... others (2017). Global warming and recurrent mass bleaching of corals. *Nature*, *543*(7645), 373–377.

Lashley, C. H., Roelvink, D., van Dongeren, A., Buckley, M. L., & Lowe, R. J. (2018). Nonhydrostatic and surfbeat model predictions of extreme wave run-up in fringing reef environments. *Coastal Engineering*, *137*, 11–27.

Lentz, S., Churchill, J., Davis, K., Farrar, J., Pineda, J., & Starczak, V. (2016). The characteristics and dynamics of wave-driven flow across a platform coral reef in the red sea. *Journal of Geophysical Research: Oceans*, *121*(2), 1360–1376.

Lowe, R. J., & Falter, J. L. (2015). Oceanic forcing of coral reefs. *Annual review of marine science*, *7*, 43–66.

Lowe, R. J., Falter, J. L., Bandet, M. D., Pawlak, G., Atkinson, M. J., Monismith, S. G., & Koseff, J. R. (2005). Spectral wave dissipation over a barrier reef. *Journal of Geophysical Research: Oceans*, *110*(C4). doi: 10.1029/2004JC002711

Lowe, R. J., Falter, J. L., Koseff, J. R., Monismith, S. G., & Atkinson, M. J. (2007). Spectral wave flow attenuation within submerged canopies: Implications for wave energy dissipation. *Journal of Geophysical Research: Oceans*, *112*(C5).

Mahabot, M.-M., Pennober, G., Suanez, S., Troadec, R., & Delacourt, C. (2017). Effect of tropical cyclones on short-term evolution of carbonate sandy beaches on reunion island, indian ocean. *Journal of Coastal Research*, *33*(4), 839–853.

McLean, R., & Kench, P. (2015). Destruction or persistence of coral atoll islands in the face of 20th and 21st century sea-level rise? *Wiley Interdisciplinary Reviews: Climate Change*, *6*(5), 445–463.

Merrifield, M., Becker, J., Ford, M., & Yao, Y. (2014). Observations and estimates of wave-driven water level extremes at the Marshall Islands. *Geophysical Research Letters*, *41*(20), 7245–7253.

Monismith, S. G., Herdman, L. M., Ahmerkamp, S., & Hench, J. L. (2013). Wave transformation and wave-driven flow across a steep coral reef. *Journal of Physical Oceanography*, *43*(7), 1356–1379.

Monismith, S. G., Rogers, J. S., Koweek, D., & Dunbar, R. B. (2015). Frictional wave dissipation on a remarkably rough reef. *Geophysical Research Letters*, *42*(10), 4063-4071. doi: 10.1002/2015GL063804

Mouquet, P., Bajjouk, T., & Ropert, M. (2016). *MNT Bathymétrique à haute résolution des fonds marins des zones récifales de la côte ouest de l'île de La Réunion (2015)* (Tech. Rep.). Ifremer délégation Océan Indien. doi: 10.12770/ee059de2-2c81-46ce-88de-0fb5517046af

Owen, S., Kench, P., & Ford, M. (2016). Improving understanding of the spatial dimensions of biophysical change in atoll island countries and implications for island communities: A marshall islands' case study. *Applied Geography*, *72*, 55–64.

Pascal, N., Allenbach, M., Brathwaite, A., Burke, L., Le Port, G., & Clua, E. (2016). Economic valuation of coral reef ecosystem service of coastal protection: A pragmatic approach. *Ecosystem Services*, *21*, 72–80.

Pearson, S., Storlazzi, C. D., Van Dongeren, A., Tissier, M., & Reniers, A. (2017). A bayesian-based system to assess wave-driven flooding hazards on coral reef-lined coasts. *Journal of Geophysical Research: Oceans*, *122*(12), 10099–10117.

Pedersen, T. (2002). *Wave measurements using the PUV method* (Technical Report No. 1). Nortek Group.

Péquignet, A.-C., Becker, J. M., Merrifield, M., & Boc, S. (2011). The dissipation of wind wave energy across a fringing reef at ipan, guam. *Coral Reefs*, *30*(1), 71–82.

Péquignet, A.-C. N., Becker, J. M., & Merrifield, M. A. (2014). Energy transfer between wind waves and low-frequency oscillations on a fringing reef, Ipan, Guam. *Journal of Geophysical Research: Oceans*, *119*(10), 6709–6724. doi: 10.1002/2014JC010179

Péquignet, A. C. N., Becker, J. M., Merrifield, M. A., & Aucan, J. (2009). Forcing of resonant modes on a fringing reef during tropical storm man-yi. *Geophysical Research Letters*, *36*(3).

Pierson, W. J., & Marks, W. (1952). The power spectrum analysis of ocean-wave records. *Eos, Transactions American Geophysical Union*, *33*(6), 834–844.

Pomeroy, A., Lowe, R., Symonds, G., Van Dongeren, A., & Moore, C. (2012). The dynamics of infragravity wave transformation over a fringing reef. *Journal of Geophysical Research: Oceans*, *117*(11).

Pomeroy, A. W., Lowe, R. J., Van Dongeren, A. R., Ghisalberti, M., Bodde, W., & Roelvink, D. (2015). Spectral wave-driven sediment transport across a fringing reef. *Coastal Engineering*, *98*, 78–94.

Principe, P., Bradley, P., Yee, S., Fisher, W., Johnson, E., Allen, P., & Campbell, D. (2011). *Quantifying coral reef ecosystem services.* U.S. Environmental Protection Agency.

Quataert, E., Storlazzi, C., Rooijen, A., Cheriton, O., & van Dongeren, A. (2015). The influence of coral reefs and climate change on wave-driven flooding of tropical coastlines. *Geophysical Research Letters*, *42*, 6407–6415. doi: 10.1002/2015GL064861.Received

Quataert, E., Storlazzi, C., van Dongeren, A., & McCall, R. (2020). The importance of explicitly modelling sea-swell waves for runup on reef-lined coasts. *Coastal Engineering*, 103704.

Roelvink, D., McCall, R., Mehvar, S., Nederhoff, K., & Dastgheib, A. (2018). Improving predictions of swash dynamics in XBeach: The role of groupiness and incident-band runup. *Coastal Engineering*, *134*, 103–123.

Roelvink, D., Reniers, A., van Dongeren, A., van Thiel de Vries, J., McCall, R., & Lescinski, J. (2009). Modelling storm impacts on beaches, dunes and barrier islands. *Coastal Engineering*, *56*(11-12), 1133–1152. doi: 10.1016/J.COASTALENG.2009.08.006

Roelvink, J. A., & Brøker, I. (1993). Cross-shore profile models. *Coastal Engineering*, *21*(1-3), 163–191.

Rogers, J. S., Monismith, S. G., Koweek, D. A., & Dunbar, R. B. (2016). Wave dynamics of a p acific a toll with high frictional effects. *Journal of Geophysical Research: Oceans*, *121*(1), 350–367.

Ropert Michel, Mouquet Pascal, Bajjouk Touria, & Delacourt Christophe. (2016). *HYSCORES : Cartographies hyperspectrales appliquées aux écosystèmes coralliens et à leur état de santé.* (Tech. Rep.). Ifremer Délegation Ocean Indien. Retrieved from `https://archimer.ifremer.fr/doc/00350/46122/https://doi.org/10.13155/46122` doi: doi.org/10.13155/46122

Rueda, A., Cagigal, L., Pearson, S., Antolínez, J. A., Storlazzi, C., van Dongeren, A., ... Mendez, F. J. (2019). Hycreww: a hybrid coral reef wave and water level metamodel. *Computers & Geosciences*, *127*, 85–90.

Scott, F., Antolinez, J. A., McCall, R., Storlazzi, C., Reniers, A., & Pearson, S. (2020). Hydro-morphological characterization of coral reefs for wave runup prediction. *Frontiers in Marine Science*, *7*, 361.

Sheppard, C., Dixon, D. J., Gourlay, M., Sheppard, A., & Payet, R. (2005). Coral mortality increases wave energy reaching shores protected by reef flats: Examples from the Seychelles. *Estuar. Coast. Shelf Sci.*, *64*(2-3), 223–234. doi: 10.1016/j.ecss.2005.02.016

Sous, D., Dodet, G., Bouchette, F., & Tissier, M. (2020). Momentum balance over a barrier reef. *Journal of Geophysical Research. Oceans*, *125*(2).

Sous, D., Tissier, M., Rey, V., Touboul, J., Bouchette, F., Devenon, J.-L., ... Aucan, J.

(2019). Wave transformation over a barrier reef. *Continental Shelf Research*, *184*, 66–80.

Storlazzi, C. D., Elias, E. P., & Berkowitz, P. (2015). Many atolls may be uninhabitable within decades due to climate change. *Scientific reports*, *5*(1), 1–9.

Storlazzi, C. D., Gingerich, S. B., van Dongeren, A., Cheriton, O. M., Swarzenski, P. W., Quataert, E., ... others (2018). Most atolls will be uninhabitable by the mid-21st century because of sea-level rise exacerbating wave-driven flooding. *Science Advances*, *4*(4), eaap9741.

Symonds, G., Black, K. P., & Young, I. R. (1995). Wave-driven flow over shallow reefs. *Journal of Geophysical Research: Oceans*, *100*(C2), 2639–2648.

Symonds, G., Huntley, D. A., & Bowen, A. J. (1982). Two-dimensional surf beat: Long wave generation by a time-varying breakpoint. *Journal of Geophysical Research: Oceans*, *87*(C1), 492–498.

UNESCO. (2014). *Islands of the future — building resilience in a changing world*. Retrieved from `https://unesdoc.unesco.org/ark:/48223/pf0000224512`

Van Dongeren, A., Lowe, R., Pomeroy, A., Trang, D. M., Roelvink, D., Symonds, G., & Ranasinghe, R. (2013). Numerical modeling of low-frequency wave dynamics over a fringing coral reef. *Coastal Engineering*, *73*, 178–190. Retrieved from `http://dx.doi.org/10.1016/j.coastaleng.2012.11.004` doi: 10.1016/j.coastaleng.2012.11.004

van Dongeren, A., Roelvink, D., McCall, R., Nederhoff, K., & van Rooijen, A. (2017). Modeling the morphological impacts of coastal storms. *Coastal storms: Processes and impacts*, 195–216.

Vetter, O., Becker, J. M., Merrifield, M. A., Pequignet, A.-C., Aucan, J., Boc, S. J., & Pollock, C. E. (2010). Wave setup over a pacific island fringing reef. *Journal of Geophysical Research: Oceans*, *115*(C12).

Woodhead, A. J., Hicks, C. C., Norström, A. V., Williams, G. J., & Graham, N. A. (2019). Coral reef ecosystem services in the anthropocene. *Functional Ecology*, *33*(6), 1023–1034.